A General Mode Matching Technique applied to Bandpass Radomes

Widenberg, Björn

2001

CODEN:LUTEDX/(TEAT-7098)/1-33/(2001)

A General Mode Matching Technique applied to Bandpass Radomes

Björn Widenberg

Department of Electroscience
Electromagnetic Theory
Lund Institute of Technology
Sweden

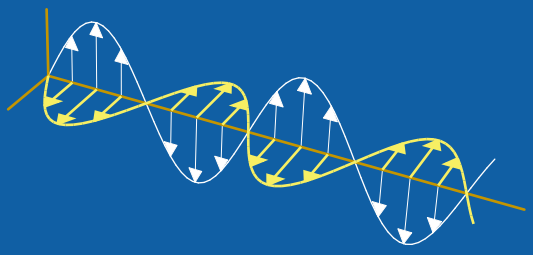

Björn Widenberg

Department of Electroscience
Electromagnetic Theory
Lund Institute of Technology
P.O. Box 118
SE-221 00 Lund
Sweden

Editor: Gerhard Kristensson

Abstract

A new method based on the mode matching technique and the finite element method (FEM) is presented. The method can handle a general thick frequency selective structure (FSS), that consists of an arbitrary number of aperture layers and dielectric layers. An aperture layer consists of a conducting plate with a periodic array of apertures. The order and the thickness of the layers can be arbitrary. The aperture can have arbitrary cross-section, and these cross-sections can be changed stepwise. The apertures can also be filled with a dielectric material.

The method for the bandpass radomes is based on general mode matching technique and cascade coupling. The fields outside the FSS and inside the dielectric layers are expanded in Floquet modes. Inside the aperture layers the fields are expanded in waveguide modes, which are calculated with FEM. By a mode matching technique, a scattering matrix is calculated for every boundary surface and a propagation matrix is calculated for every layer. These matrices are cascade coupled to form a scattering matrix for the complete FSS. The method has been verified by comparison with other methods and measurements.

1 Introduction

In this paper general thick Frequency Selective Structures (FSS) are studied by a general mode matching technique. There are two major applications of FSS. One is to use FSS as antenna radomes for better control of electromagnetic wave transmission and scattering. A radome is a cover designed to protect an antenna from the effects of its physical environment without degrading its electric performance. The other application of FSS is in reflector antenna systems, there FSS reflectors are used to separate feeds of different frequency bands.

Bandpass radomes are most often constructed from one or more metallic screens that are sandwiched between dielectric slabs. The metallic screens are perforated in a regular pattern such that at the resonant frequency of the structure, the radome passes nearly 100% of the incident power. Outside the passband, nearly all of the incident power is reflected. In essence, these radomes provide a bandpass filter function to the antennas located behind them.

Bandpass radomes contain elements in a regular grid pattern that are formed in an electrically conductive plate. In the analysis of thick-screen frequency selective surfaces (FSS), one cannot neglect the thickness of the element, as is the case with thin-screen FSSs.

An earlier study on thick FSS can be found in [11] by Widenberg, Poulsen and Karlsson. In the book edited by Wu [12], an equivalent problem for the thick-screen FSS is analyzed. By employing a spectral moment method solution to the magnetic field integral equation, Wu determines the transmission and reflection. Munk has also studied the problem of thick FSS in his book [5].

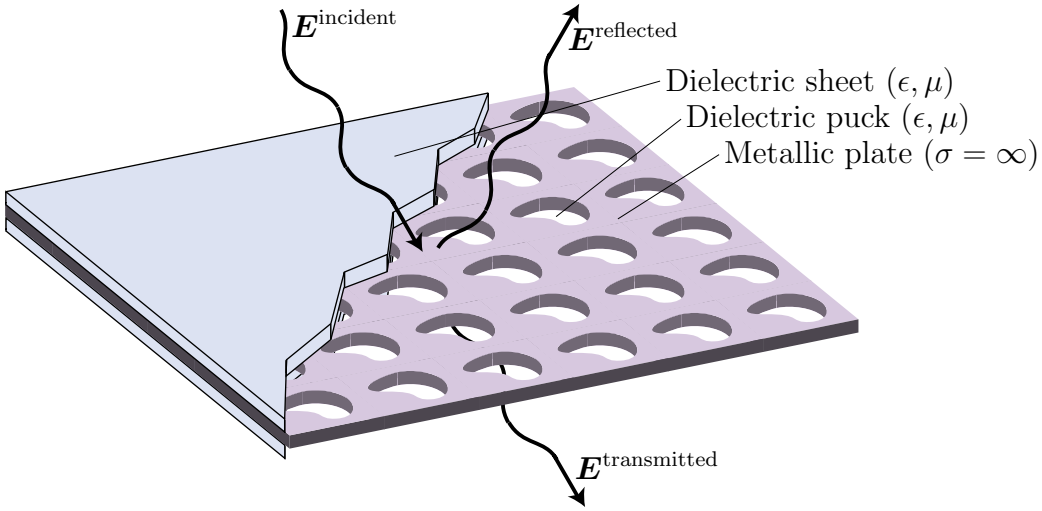

Figure 1: A Bandpass Radome.

2 The geometry of the FSS

The geometry of the thick-screen FSS is depicted in Figure 1. The screen consists of an arbitrary number of aperture layers and dielectric layers. The order and the thickness of the layers can be arbitrary. An aperture layer consists of a conducting plate perforated with a periodic array of apertures. Every element in the aperture layer is assumed to be a waveguide element. In any cut through a plane parallel to the xy-plane the waveguides are identical but with an arbitrary shape, and the shape of the element is fixed along the z-axis. The apertures can be filled with a dielectric material and any number of dielectric layers is allowed on either side of the conductive thick screen.

The FSS is assumed to extend infinitely in the xy-plane. The grid for the periodic structure is defined in Figure 2. The z-axis is assumed to be orthogonal to the surface of the perfectly conducting screen. These apertures are spaced periodically along the x-axis with period a. The other axis of periodicity y' makes an angle ϕ_0 with the x-axis and the apertures are spaced periodically along this second axis with period b, see Figure 2. Hence, the array of apertures is divided into identical cells. The cell at the origin is called the unit cell, and is denoted $D \in \mathbb{R}^2$. The area of the unit cell is defined as $A_D := ab \sin \phi_0$. The cross-section of the aperture at the unit cell is denoted $\Omega \in \mathbb{R}^2$, $\Omega \subset D$.

Figure 3 shows several possible unit elements for application in a thick-screen FSS. The element in Figure 3(a) is a simple waveguide through a conducting plate, which is sometimes referred to as a Puck Plate (PP) because of the high dielectric ceramic pucks that are often used to load the waveguide. Figure 3(b) shows a coaxial puck plate FSS, where the element is a coaxial waveguide, [8]. The element in Figure 3(c) composes the Artificial Puck Plate (APP) bandpass radome, [9], which have conductive paths that form irises at the aperture on either side of the screen.

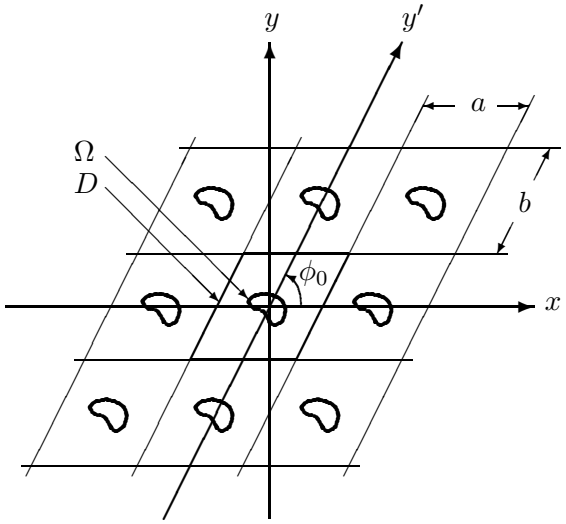

Figure 2: The periodicity of the FSS.

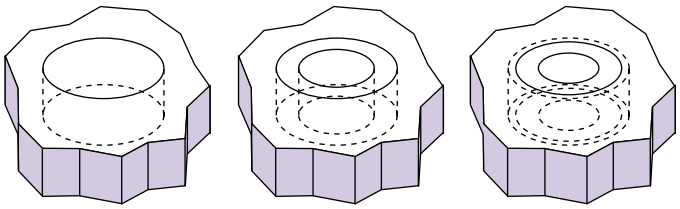

Figure 3: Some possible unit elements for thick-screen FSS applications.

In this paper the geometry of the aperture is arbitrary. This is possible since the method does not rely on explicit expressions for the waveguide modes. Instead FEM is used to obtain appropriate waveguide modes. A number of different apertures, which can be investigated in numerical calculations by the current method, are shown in Figure 4. The apertures in the figure are, from left, rectangular-, circular-, hexagonal-, cross-, tripole-, rectangular loop-, annular-, hexagonal loop-, cross loop- and tripole loop apertures.

Figure 4: Some possible cross-sections for the apertures.

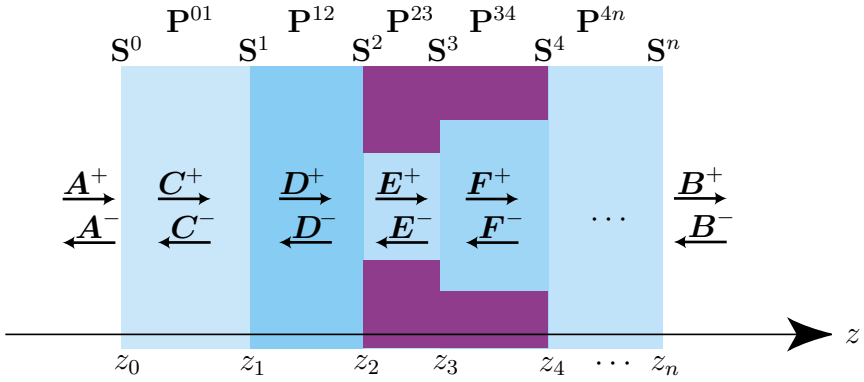

Figure 5: A cross-section of a frequency selective structure.

3 The Method

The method for the frequency selective structure is based on general mode matching technique and cascade coupling. The method has been used in many different areas, *e.g.*, for waveguide discontinuities [10] and horn antennas [6].

A plane wave impinges on the FSS, and the reflection and transmission coefficients are computed. According to the Floquet's theorem it is sufficient to study one unit cell D, because there is only a difference of the phase between the sides of the unit cell. The FSS is divided into a number of layers, see Figure 5. The fields outside the FSS and inside the dielectric layers are expanded in tangential plane waves, *i.e.*, Floquet waves. Inside the aperture layers the fields are expanded in waveguide modes which are calculated by FEM. The tangential electric and magnetic fields are matched by the boundary conditions at every boundary surface of the structure in order to obtain a scattering matrix $\mathbf{S}$, see Figure 5. For every layer a propagation matrix $\mathbf{P}$ is calculated. These scattering matrices are cascade coupled to form a scattering matrix for the complete FSS, see Figure 6. The transmitted and reflected fields are calculated from this scattering matrix.

In Section 4 the mode matching technique and the cascade coupling are described. The expansion of the fields in the different layers is described in Section 5.

4 The Mode Matching Technique

The mode-matching technique is a powerful method for analyzing periodic structures and waveguides with varying cross-section. The actual profile is replaced by a series of uniform layers. Hence, it is ideal for the analysis of thick frequency selective structures.

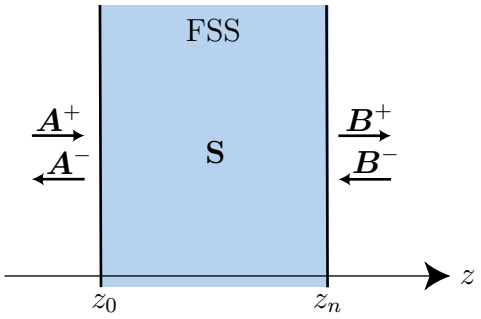

Figure 6: Frequency selective structure represented as a scattering matrix.

4.1 Principles of Mode Matching Technique

In a waveguide or periodic structure the field can be expanded in a complete set of vector wave functions, these functions are usually denoted modes. The mode matching technique is based on the matching of the total mode fields at each junction between uniform sections. The amplitudes of the separate modes at the output of a junction can be deduced in terms of the amplitudes of the mode spectrum at the input to the junction. The strength of the modal-matching technique stems from the fact that the amplitudes of the modes can be expressed as the components of a scattering matrix. Each junction along the FSS has its own scattering matrix. The matrices for all junctions can be cascaded and results in an overall scattering matrix for the FSS. The process of computing the overall scattering matrix can be decoupled from the process of obtaining the elements of a particular scattering matrix.

The concept of matching modes at a junction was first attempted in the late 1960s [10] and early 1970s [4]. Because of the limited computer power available at that time it was not possible to do more than simple computations. The computational emphasis was on reducing the number of modes to the minimum so that a numerical solution could be obtained. It was the arrival of powerful computers that enabled the concept to be applied to the analysis of complicated structures.

4.2 The Scattering Matrix

This section describes the modal-matching technique in general terms, applicable to any specific waveguide or frequency selective structure.

The modal-matching technique can be used to obtain the overall transmission and reflection properties of an FSS. The FSS is represented as a layer, see Figure 6, where $\boldsymbol{A}^+$ and $\boldsymbol{B}^-$ are column matrices containing the mode coefficients of the total incident field. The column matrices $\boldsymbol{A}^-$ and $\boldsymbol{B}^+$ contain the mode coefficients of the total scattered field. The characteristics of the FSS are given by a scattering

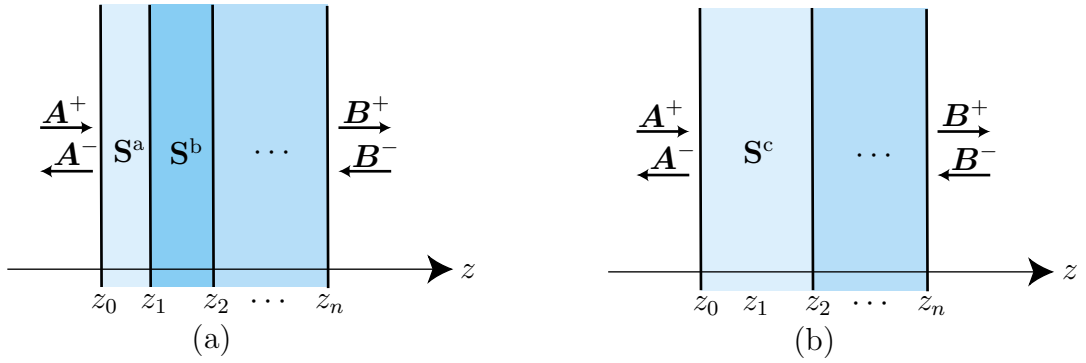

Figure 7: Cascading of scattering matrices.

matrix $\mathbf{S}$,

$$\begin{pmatrix} \boldsymbol{A}^- \\ \boldsymbol{B}^+ \end{pmatrix} = \mathbf{S} \begin{pmatrix} \boldsymbol{A}^+ \\ \boldsymbol{B}^- \end{pmatrix} = \begin{pmatrix} \mathbf{S}_{11} & \mathbf{S}_{12} \\ \mathbf{S}_{21} & \mathbf{S}_{22} \end{pmatrix} \begin{pmatrix} \boldsymbol{A}^+ \\ \boldsymbol{B}^- \end{pmatrix}. \tag{4.1}$$

The elements of $\mathbf{S}$ describe the coupling between the modes on the left-hand side with the modes on the right-hand side of the FSS.

If there is no source on the right-hand side, *i.e.*, $\boldsymbol{B}^- = \mathbf{0}$, the reflection coefficient for the FSS is

$$\boldsymbol{A}^- = \mathbf{S}_{11}\boldsymbol{A}^+, \tag{4.2}$$

i.e., $\mathbf{S}_{11}$ is the reflection matrix. The transmission matrix of the FSS is then $\mathbf{S}_{21}$ since

$$\boldsymbol{B}^+ = \mathbf{S}_{21}\boldsymbol{A}^+. \tag{4.3}$$

The length of the column matrices and the size of the scattering matrix depend on the number of modes at each side of the FSS. If there are n_{a} modes on the left-hand side and n_{b} on the right-hand side, the length of $\boldsymbol{A}^{\pm}$ are n_{a} and the length of $\boldsymbol{B}^{\pm}$ are n_{b}. The size of the scattering matrix $\mathbf{S}$ is $(n_{\mathrm{a}} + n_{\mathrm{b}}) \times (n_{\mathrm{a}} + n_{\mathrm{b}})$ and the sizes of the submatrices are $\mathbf{S}_{11}:\ n_{\mathrm{a}} \times n_{\mathrm{a}}$, $\mathbf{S}_{12}:\ n_{\mathrm{a}} \times n_{\mathrm{b}}$, $\mathbf{S}_{21}:\ n_{\mathrm{b}} \times n_{\mathrm{a}}$, and $\mathbf{S}_{22}:\ n_{\mathrm{b}} \times n_{\mathrm{b}}$.

4.3 Cascading of Scattering Matrices

The FSS is divided into a number of boundaries and layers. For instance, the FSS shown in Figure 1 has four boundaries and three layers. Each boundary or layer can be represented by its own scattering matrix defined as in Equation 4.1 and Figure 6. The scattering matrix $\mathbf{S}$ represents the scattering properties of the individual boundary or layer. By an iterative method, the scattering matrix of the complete FSS is formed from the individual scattering matrices. The first step in this iteration is indicated in Figure 7.

Scattering matrices are particularly useful because it is straightforward to cascade two scattering matrices, see Appendix A.2. If these two scattering matrices have elements

$$\mathbf{S}^{\mathrm{a}} = \begin{pmatrix} \mathbf{S}^{\mathrm{a}}_{11} & \mathbf{S}^{\mathrm{a}}_{12} \\ \mathbf{S}^{\mathrm{a}}_{21} & \mathbf{S}^{\mathrm{a}}_{22} \end{pmatrix} \quad \text{and} \quad \mathbf{S}^{\mathrm{b}} = \begin{pmatrix} \mathbf{S}^{\mathrm{b}}_{11} & \mathbf{S}^{\mathrm{b}}_{12} \\ \mathbf{S}^{\mathrm{b}}_{21} & \mathbf{S}^{\mathrm{b}}_{22} \end{pmatrix}, \tag{4.4}$$

then the cascaded scattering matrix is

$$\mathbf{S}^{\mathrm{c}} = \begin{pmatrix} \mathbf{S}^{\mathrm{c}}_{11} & \mathbf{S}^{\mathrm{c}}_{12} \\ \mathbf{S}^{\mathrm{c}}_{21} & \mathbf{S}^{\mathrm{c}}_{22} \end{pmatrix}. \tag{4.5}$$

The matrix element are given by

$$\begin{cases} \mathbf{S}^{\mathrm{c}}_{11} = \mathbf{S}^{\mathrm{a}}_{11} + \mathbf{S}^{\mathrm{a}}_{12}(\mathbf{I} - \mathbf{S}^{\mathrm{b}}_{11}\mathbf{S}^{\mathrm{a}}_{22})^{-1}\mathbf{S}^{\mathrm{b}}_{11}\mathbf{S}^{\mathrm{a}}_{21}, \\ \mathbf{S}^{\mathrm{c}}_{12} = \mathbf{S}^{\mathrm{a}}_{12}(\mathbf{I} - \mathbf{S}^{\mathrm{b}}_{11}\mathbf{S}^{\mathrm{a}}_{22})^{-1}\mathbf{S}^{\mathrm{b}}_{12}, \\ \mathbf{S}^{\mathrm{c}}_{21} = \mathbf{S}^{\mathrm{b}}_{21}(\mathbf{I} - \mathbf{S}^{\mathrm{a}}_{22}\mathbf{S}^{\mathrm{b}}_{11})^{-1}\mathbf{S}^{\mathrm{a}}_{21}, \\ \mathbf{S}^{\mathrm{c}}_{22} = \mathbf{S}^{\mathrm{b}}_{22} + \mathbf{S}^{\mathrm{b}}_{21}(\mathbf{I} - \mathbf{S}^{\mathrm{a}}_{22}\mathbf{S}^{\mathrm{b}}_{11})^{-1}\mathbf{S}^{\mathrm{a}}_{22}\mathbf{S}^{\mathrm{b}}_{12}, \end{cases} \tag{4.6}$$

where $\mathbf{I}$ is a unit matrix. The size of the cascaded scattering matrix $\mathbf{S}^{\mathrm{c}}$ is $(n_{\mathrm{a}} + n_{\mathrm{c}}) \times (n_{\mathrm{a}} + n_{\mathrm{c}})$, where the sizes of the submatrices are $\mathbf{S}^{c}_{11}:\ n_{\mathrm{a}} \times n_{\mathrm{a}}$, $\mathbf{S}^{c}_{12}:\ n_{\mathrm{a}} \times n_{\mathrm{c}}$, $\mathbf{S}^{c}_{21}:\ n_{\mathrm{c}} \times n_{\mathrm{a}}$, and $\mathbf{S}^{c}_{22}:\ n_{\mathrm{c}} \times n_{\mathrm{c}}$.

The cascading process has the advantage that the exact number of layers does not have to be known at the start of the analysis as the process proceeds from one side to the other side in a logical fashion.

In order to determine the scattering matrices of the separate boundaries and uniform sections, see Section 6, the fields must be expanded in appropriate basis functions.

5 Expansion of the fields

In Figure 8 a simple FSS is depicted, which consists of a perforated conducting plate sandwiched between two dielectric slabs. A plane wave $\boldsymbol{E}^{\mathrm{in}}$, with wave vector

$$\boldsymbol{k}_0 := \hat{x}k_0 \sin\theta\cos\phi + \hat{y}k_0 \sin\theta\sin\phi + \hat{z}k_0\cos\theta = \hat{x}k_{0\mathrm{x}} + \hat{y}k_{0\mathrm{y}} + \hat{z}k_{0\mathrm{z}}, \tag{5.1}$$

impinges on the screen. Here, θ and ϕ are the spherical angles of incidence, that is θ is the polar angle measured from the z-axis and ϕ is the azimuthal angle measured from the x-axis towards the y-axis. The wave number k_0 is given by $k_0 := \omega/c_0$, where $\omega := 2\pi f$, f is the frequency, and c_0 is the speed of light in vacuum. The scattered fields are discrete sums of plane waves, *cf.* Figure 8, where some of these are propagating waves, while others are evanescent waves. The scattered field consist of at least two propagating plane waves, one of which propagate in the reflected direction, and one of which in the transmitted direction.

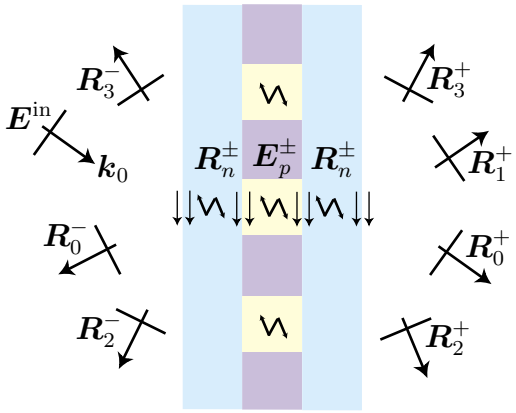

Figure 8: Expansion of the fields.

Outside the structure and inside the dielectric layers the transverse electric and magnetic fields are expanded as

$$\begin{cases} \boldsymbol{E}_{\mathrm{T}}^{\mathrm{d}}(\boldsymbol{r}) = \sum\limits_{lmn} (a_{lmn}^{+} \mathrm{e}^{\mathrm{i}\gamma_{mn}z} + a_{lmn}^{-} \mathrm{e}^{-\mathrm{i}\gamma_{mn}z}) \boldsymbol{R}_{\mathrm{T}lmn}(\boldsymbol{\rho}), \\ \boldsymbol{H}_{\mathrm{T}}^{\mathrm{d}}(\boldsymbol{r}) = \sum\limits_{lmn} (a_{lmn}^{+} \mathrm{e}^{\mathrm{i}\gamma_{mn}z} - a_{lmn}^{-} \mathrm{e}^{-\mathrm{i}\gamma_{mn}z}) \boldsymbol{T}_{\mathrm{T}lmn}(\boldsymbol{\rho}), \end{cases} \tag{5.2}$$

where $\boldsymbol{R}_{\mathrm{T}lmn}$ and $\boldsymbol{T}_{\mathrm{T}lmn}$ are Floquet mdes, *cf.* Subsection 5.1. The transverse electric and magnetic fields inside the waveguide layers, see Figure 8, are expanded as

$$\begin{cases} \boldsymbol{E}_{\mathrm{T}}^{\mathrm{w}}(\boldsymbol{r}) = \sum\limits_{vn} (a_{vn}^{+} \mathrm{e}^{\mathrm{i}k_{zn}z} + a_{vn}^{-} \mathrm{e}^{-\mathrm{i}k_{zn}z}) \boldsymbol{E}_{\mathrm{T}vn}(\boldsymbol{\rho}), \\ \boldsymbol{H}_{\mathrm{T}}^{\mathrm{w}}(\boldsymbol{r}) = \sum\limits_{vn} (a_{vn}^{+} \mathrm{e}^{\mathrm{i}k_{zn}z} - a_{vn}^{-} \mathrm{e}^{-\mathrm{i}k_{zn}z}) \boldsymbol{H}_{\mathrm{T}vn}(\boldsymbol{\rho}), \end{cases} \tag{5.3}$$

where $\boldsymbol{E}_{\mathrm{T}vn}$ and $\boldsymbol{H}_{\mathrm{T}vn}$ are waveguide modes, *cf.* Subsection 5.2.

5.1 The Floquet Modes

Introduce the transverse vector

$$\boldsymbol{\tau}_{mn} := \hat{x}\alpha_m + \hat{y}\beta_{mn}, \tag{5.4}$$

where the Floquet mode indices are given by

$$\alpha_m := \frac{2\pi m}{a} + k_{0x}, \qquad \beta_{mn} := \frac{2\pi n}{b \sin\phi_0} - \frac{2\pi m}{a} \cot\phi_0 + k_{0y}. \tag{5.5}$$

The Floquet modes are periodic vector valued functions and defined as

$$\begin{aligned}\boldsymbol{R}_{\mathrm{T}lmn}(\boldsymbol{\rho}) &= \begin{cases}(\hat{\tau}_{mn}\times\hat{z})\dfrac{1}{\sqrt{A_D}}\mathrm{e}^{\mathrm{i}\boldsymbol{\tau}_{mn}\cdot\boldsymbol{\rho}}, & l=1,\\ \hat{\tau}_{mn}\dfrac{1}{\sqrt{A_D}}\mathrm{e}^{\mathrm{i}\boldsymbol{\tau}_{mn}\cdot\boldsymbol{\rho}}, & l=2,\end{cases}\\ \boldsymbol{T}_{\mathrm{T}lmn}(\boldsymbol{\rho}) &= \frac{Y_{lmn}}{\eta_0}\hat{z}\times\boldsymbol{R}_{\mathrm{T}lmn},\end{aligned} \tag{5.6}$$

where $\boldsymbol{\rho} := \hat{x}x + \hat{y}y$, A_D is the area of the unit cell and where

$$Y_{lmn} = \begin{cases}\frac{\gamma_{mn}}{\mu k_0}, & l=1,\\ \frac{\epsilon k_0}{\gamma_{mn}}, & l=2.\end{cases} \tag{5.7}$$

are the wave admittance for the Floquet modes. For $l=1$ and $l=2$, $\boldsymbol{R}_{\mathrm{T}lmn}(\boldsymbol{r})$ represent TE and TM polarized waves, respectively. Notice that the Floquet mode $\boldsymbol{R}_{\mathrm{T}lmn}$ represents the electric field, and $\boldsymbol{T}_{\mathrm{T}lmn}$ represents the magnetic field.

The Floquet modes are tangential plane waves, and they are orthonormal to each other in the sense that

$$\int_D \boldsymbol{R}_{\mathrm{T}lmn}(\boldsymbol{\rho})\cdot\boldsymbol{R}^*_{\mathrm{T}l'm'n'}(\boldsymbol{\rho})\,\mathrm{d}x\,\mathrm{d}y = \delta_{ll'}\delta_{mm'}\delta_{nn'}, \tag{5.8}$$

where $*$ denotes complex conjugate. From (5.6), the relation between $\boldsymbol{R}_{\mathrm{T}lmn}$ and $\boldsymbol{T}_{\mathrm{T}lmn}$ can also be written as

$$\eta_0\boldsymbol{T}_{\mathrm{T}lmn}\times\hat{z} = Y_{lmn}\boldsymbol{R}_{\mathrm{T}lmn}. \tag{5.9}$$

The relation

$$k^2 = k_{\mathrm{x}}^2 + k_{\mathrm{y}}^2 + k_{\mathrm{z}}^2 = \alpha_m^2 + \beta_{mn}^2 + \gamma_{mn}^2, \tag{5.10}$$

defines γ_{mn} and the principal square root branch is chosen such that the imaginary part of γ_{mn} is non-negative.

The Floquet waves are related to the tangential Floquet modes as

$$\begin{aligned}\boldsymbol{R}^{\pm}(\boldsymbol{r}) &= \begin{cases}\boldsymbol{R}_{\mathrm{T}}(\boldsymbol{\rho})\mathrm{e}^{\pm\mathrm{i}\gamma z}, & l=1,\\ (\hat{\tau}\mp\hat{z}\frac{\tau}{\gamma})R_{\mathrm{T}}(\boldsymbol{\rho})\mathrm{e}^{\pm\mathrm{i}\gamma z}, & l=2,\end{cases}\\ \eta\boldsymbol{T}^{\pm}(\boldsymbol{r}) &= \frac{1}{\mathrm{i}k}\nabla\times\boldsymbol{R}^{\pm}(\boldsymbol{r}).\end{aligned} \tag{5.11}$$

The derivation of the z-component from the tangential component can be found in [11]. The z-dependence indicate that $\boldsymbol{R}^+$ and $\boldsymbol{R}^-$ propagate in the positive and negative z-direction, respectively.

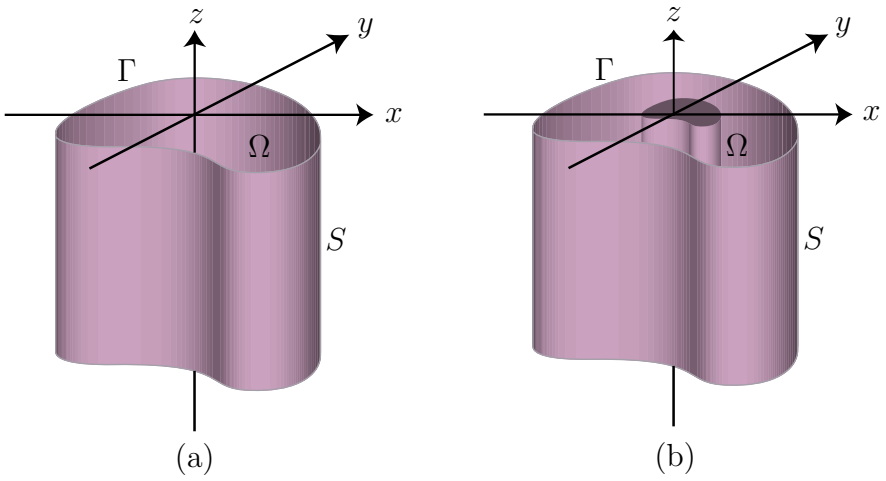

Figure 9: Geometry for a waveguide

5.2 The Waveguide Modes

The geometry for a cylindric waveguide with arbitrary cross-section is depicted in Figure 9. Standard waveguide theory, see *e.g.*, [1], gives that the z-dependence of all field vectors in the waveguide is given by $\mathrm{e}^{\pm \mathrm{i}k_{\mathrm{z}}z}$, where k_{z} is the propagation constant and the $+$ $(-)$ sign indicates propagation along the positive (negative) z-direction. In a waveguide, the total electric and magnetic fields are decomposed in the following way

$$\begin{aligned} \boldsymbol{E}^{\pm}(\boldsymbol{r},\omega) &= (\boldsymbol{E}_{\mathrm{T}}(\boldsymbol{\rho},\omega) \pm \hat{z}E_{\mathrm{z}}(\boldsymbol{\rho}))\mathrm{e}^{\pm \mathrm{i}k_{\mathrm{z}}z}, \\ \eta_0\boldsymbol{H}^{\pm}(\boldsymbol{r},\omega) &= (\pm\eta_0\boldsymbol{H}_{\mathrm{T}}(\boldsymbol{\rho},\omega) + \hat{z}H_{\mathrm{z}}(\boldsymbol{\rho}))\mathrm{e}^{\pm \mathrm{i}k_{\mathrm{z}}z}. \end{aligned} \tag{5.12}$$

In the waveguide in Figure 9(a) two different modes, the transverse electric (TE) mode and the transverse magnetic (TM) mode, can exist. In the waveguide with an inner conductor, *cf.* Figure 9(b), the transverse electromagnetic (TEM) mode can also exist. Thus $H_{\mathrm{z}} = 0$ for the TM modes, $E_{\mathrm{z}} = 0$ for the TE modes, and both $H_{\mathrm{z}} = 0$ and $E_{\mathrm{z}} = 0$ for the TEM mode.

For a homogeneous hollow waveguide, the waveguide modes are derived from the eigenvalue problem, see *e.g.*, [3], given by Helmholtz' equation,

$$\nabla_{\mathrm{T}}^2\Phi_{vn}(\boldsymbol{\rho}) + k_{tvn}^2\Phi_{vn}(\boldsymbol{\rho}) = 0, \qquad \boldsymbol{\rho} \in \Omega, \tag{5.13}$$

and the boundary conditions. Here $k_{tvn}^2 = k^2 - k_{zvn}^2$, where $k = k_0\sqrt{\epsilon\mu}$, and ∇_{T}^2 is the transverse part of the ∇^2-operator. For the TM-case ($v = 2$), $\Phi_{2n}(\boldsymbol{\rho}) = E_{\mathrm{z}2n}(\boldsymbol{\rho})$ and the solution must fulfill the Dirichlet boundary condition $\Phi_{2n}(\boldsymbol{\rho}) = 0$ at the metallic walls, while for the TE-case ($v = 1$), $\Phi_{1n}(\boldsymbol{\rho}) = H_{\mathrm{z}1n}(\boldsymbol{\rho})$ and the solution must fulfill the Neumann boundary condition $\dfrac{\partial\Phi_{1n}}{\partial n}(\boldsymbol{\rho}) = 0$ at the perfectly conducting walls. The eigenmode for the TEM-case ($v = 0$) is derived from the Laplace equation, with a Dirichlet boundary condition $\Phi(\boldsymbol{\rho}) = \Phi_i$, where Φ_i is a real constant, at the different parts of the metallic walls.

The transverse eigenmodes for TE- and TM-modes are given by

$$\begin{aligned}\boldsymbol{E}_{\mathrm{T}vn}(\boldsymbol{\rho},\omega) &= \frac{\mathrm{i}}{k_{tvn}^2(\omega)}(k_{zvn}(\omega)\nabla_{\mathrm{T}}E_{zvn}(\boldsymbol{\rho}) - k(\omega)\eta(\omega)\hat{z}\times\nabla_{\mathrm{T}}H_{zvn}(\boldsymbol{\rho})),\\ \eta_0\boldsymbol{H}_{\mathrm{T}vn}(\boldsymbol{\rho},\omega) &= \frac{\mathrm{i}}{k_{tvn}^2(\omega)}(k_{zvn}(\omega)\nabla_{\mathrm{T}}H_{zvn}(\boldsymbol{\rho}) + k(\omega)\frac{1}{\eta(\omega)}\hat{z}\times\nabla_{\mathrm{T}}E_{zvn}(\boldsymbol{\rho})),\end{aligned} \tag{5.14}$$

where $\eta = \sqrt{\frac{\mu}{\epsilon}}$, and for TEM-modes

$$\begin{aligned}\boldsymbol{E}_{\mathrm{T}0n}(\boldsymbol{\rho},\omega) &= -\nabla_{\mathrm{T}}\Phi_(\boldsymbol{\rho}),\\ \eta_0\boldsymbol{H}_{\mathrm{T}0n}(\boldsymbol{\rho},\omega) &= -\frac{1}{\eta(\omega)}\hat{z}\times\nabla_{\mathrm{T}}\Phi(\boldsymbol{\rho}).\end{aligned} \tag{5.15}$$

The transverse magnetic waveguide modes can be expressed in transverse electric waveguide modes as

$$\boldsymbol{H}_{\mathrm{T}vn}(\boldsymbol{\rho},\omega) = \frac{Y_{vn}^i}{\eta_0}\hat{z}\times\boldsymbol{E}_{\mathrm{T}vn}(\boldsymbol{\rho},\omega), \tag{5.16}$$

where

$$Y_{vn}^i = \begin{cases}\sqrt{\frac{\epsilon_i}{\mu_i}}, & v = 0 \text{ (TEM)},\\ \frac{k_{zn}^i}{\mu_i k_0}, & v = 1 \text{ (TE)},\\ \frac{\epsilon_i k_0}{k_{zn}^i}, & v = 2 \text{ (TM)},\end{cases} \tag{5.17}$$

is the admittance for the waveguide modes.

The sets of waveguide modes $\{\boldsymbol{E}_{\mathrm{T}vn}\}_{n=1}^{\infty}$ are complete and orthogonal, and the modes are normalized as

$$\int_{\Omega}\boldsymbol{E}_{\mathrm{T}vn}(\boldsymbol{\rho})\cdot\boldsymbol{E}_{\mathrm{T}v'n'}^*(\boldsymbol{\rho})\,\mathrm{d}x\,\mathrm{d}y = \delta_{vv'}\delta_{nn'}, \tag{5.18}$$

where $*$ denotes complex conjugate.

In Figure 4, a number of examples of cross-sections for a waveguide are depicted. For simple geometries, *e.g.*, rectangular, circular and annular, there are well-known analytic expressions for the waveguide modes, *cf.* [1]. Structures with rectangular apertures are treated in [7] and structures with circular apertures with an inner conductor are treated in [8]. For waveguides with more complicated cross-sections, *e.g.*, hexagonal, cross and tripole, there are generally no closed form expressions for the waveguide fields. Instead these fields need to be determined numerically, and in this paper FEM is utilized for this purpose.

6 The Scattering Matrices

In this section the scattering matrices for the different boundaries and uniform sections are determined. For an FSS there are three types of boundaries:

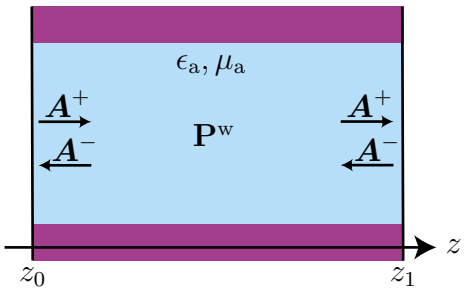

Figure 10: Propagation in a waveguide.

- Interface between two dielectric layers,
- Interface between a dielectric layer and an aperture layer,
- Interface between two aperture layers (a junction),

and two types of uniform sections:

- Dielectric layer,
- Aperture layer (a uniform section, a uniform waveguide).

6.1 Scattering Matrix of a Uniform Section

Figure 10 shows propagation through a uniform waveguide, *i.e.*, a uniform section. The scattering coefficients on each side of the section are related to each other by

$$\begin{cases} A^+_{vn}(z_1) = \mathbf{I}\mathrm{e}^{\mathrm{i}k_{zn}(z_1-z_0)}A^+_{vn}(z_0), \\ A^-_{vn}(z_1) = \mathbf{I}\mathrm{e}^{-\mathrm{i}k_{zn}(z_1-z_0)}A^-_{vn}(z_0), \end{cases} \tag{6.1}$$

which can be written in matrix form as

$$\begin{pmatrix} \boldsymbol{A}^-(z_0) \\ \boldsymbol{A}^+(z_1) \end{pmatrix} = \underbrace{\begin{pmatrix} \mathbf{0} & \mathbf{E}^{\rm w}(z_1-z_0) \\ \mathbf{E}^{\rm w}(z_1-z_0) & \mathbf{0} \end{pmatrix}}_{\mathbf{P}^{\rm w}} \begin{pmatrix} \boldsymbol{A}^+(z_0) \\ \boldsymbol{A}^-(z_1) \end{pmatrix}, \tag{6.2}$$

where

$$\mathbf{E}^{\rm w}_{vn,v'n'}(z) = \mathrm{e}^{\mathrm{i}k_{zn}z}\delta_{vv'}\delta_{nn'}. \tag{6.3}$$

A substantial number of evanescent modes must be included in the analysis. This is because the uniform section will be relatively short in length so that the decaying modes are not negligible at the next junction.

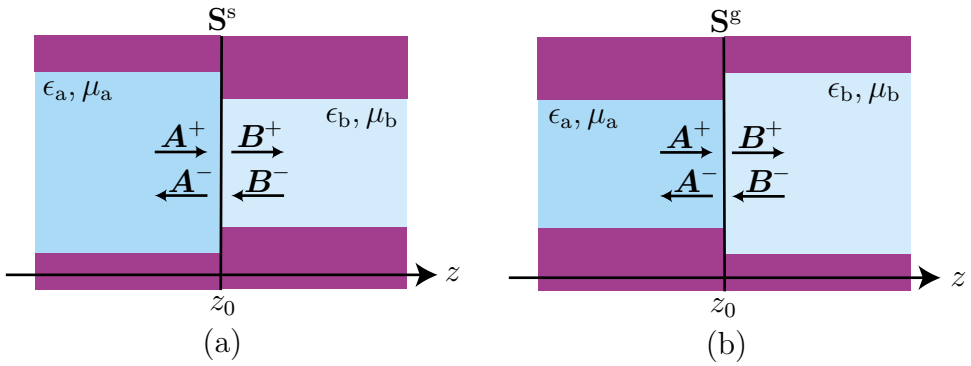

Figure 11: Interfaces between waveguides.

6.2 Scattering Matrix of a Junction

First the case with the larger waveguide on the left-hand side and the smaller waveguide on the right-hand side, see Figure 11(a), is studied.

The electric and magnetic fields inside the two waveguide sections are expanded in waveguide modes as

$$\begin{cases} \boldsymbol{E}_{\mathrm{T}}^{\mathrm{a}}(\boldsymbol{r}) = \sum\limits_{vn} (a_{vn}^{+} \mathrm{e}^{\mathrm{i}k_{zn}^{\mathrm{a}} z} + a_{vn}^{-} \mathrm{e}^{-\mathrm{i}k_{zn}^{\mathrm{a}} z}) \boldsymbol{E}_{\mathrm{T}vn}^{\mathrm{a}}(\boldsymbol{\rho}), \\ \boldsymbol{H}_{\mathrm{T}}^{\mathrm{a}}(\boldsymbol{r}) = \sum\limits_{vn} (a_{vn}^{+} \mathrm{e}^{\mathrm{i}k_{zn}^{\mathrm{a}} z} - a_{vn}^{-} \mathrm{e}^{-\mathrm{i}k_{zn}^{\mathrm{a}} z}) \boldsymbol{H}_{\mathrm{T}vn}^{\mathrm{a}}(\boldsymbol{\rho}), \end{cases} \quad z < z_0,$$
$$\begin{cases} \boldsymbol{E}_{\mathrm{T}}^{\mathrm{b}}(\boldsymbol{r}) = \sum\limits_{vn} (b_{vn}^{+} \mathrm{e}^{\mathrm{i}k_{zn}^{\mathrm{b}} z} + b_{vn}^{-} \mathrm{e}^{-\mathrm{i}k_{zn}^{\mathrm{b}} z}) \boldsymbol{E}_{\mathrm{T}vn}^{\mathrm{b}}(\boldsymbol{\rho}), \\ \boldsymbol{H}_{\mathrm{T}}^{\mathrm{b}}(\boldsymbol{r}) = \sum\limits_{vn} (b_{vn}^{+} \mathrm{e}^{\mathrm{i}k_{zn}^{\mathrm{b}} z} - b_{vn}^{-} \mathrm{e}^{-\mathrm{i}k_{zn}^{\mathrm{b}} z}) \boldsymbol{H}_{\mathrm{T}vn}^{\mathrm{b}}(\boldsymbol{\rho}), \end{cases} \quad z > z_0, \tag{6.4}$$

The boundary conditions at the interface $z = z_0$ are enforced. The boundary conditions say that the tangential electric field is continuous over the entire surface Ω_{a}, while the tangential magnetic field is continuous over the joint surface Ω_{b}, *i.e.*,

$$\begin{aligned} \boldsymbol{E}_{\mathrm{T}}^{\mathrm{a}}(\boldsymbol{\rho}, z_0) &= \begin{cases} \boldsymbol{E}_{\mathrm{T}}^{\mathrm{b}}(\boldsymbol{\rho}, z_0), & \boldsymbol{\rho} \in \Omega_{\mathrm{b}}, \\ \boldsymbol{0}, & \boldsymbol{\rho} \in \Omega_{\mathrm{a}} \setminus \Omega_{\mathrm{b}}, \end{cases} \\ \boldsymbol{H}_{\mathrm{T}}^{\mathrm{a}}(\boldsymbol{\rho}, z_0) &= \boldsymbol{H}_{\mathrm{T}}^{\mathrm{b}}(\boldsymbol{\rho}, z_0), \quad \boldsymbol{\rho} \in \Omega_{\mathrm{b}}. \end{aligned} \tag{6.5}$$

Introducing

$$\begin{aligned} A_{vn}^{\pm}(z) &= a_{vn}^{\pm} \mathrm{e}^{\pm \mathrm{i}k_{zn}^{\mathrm{a}} z}, \\ B_{vn}^{\pm}(z) &= b_{vn}^{\pm} \mathrm{e}^{\pm \mathrm{i}k_{zn}^{\mathrm{b}} z}, \end{aligned} \tag{6.6}$$

and enforcing the boundary conditions of the fields at the interface $z = z_0$ yield

$$\begin{aligned}
\sum_{vn}(A^{+}_{vn}(z_0) + A^{-}_{vn}(z_0))\boldsymbol{E}^{\mathrm{a}}_{\mathrm{T}vn}(\boldsymbol{\rho}) &= \begin{cases} \sum_{vn}(B^{+}_{vn}(z_0) + B^{-}_{vn}(z_0))\boldsymbol{E}^{\mathrm{b}}_{\mathrm{T}vn}(\boldsymbol{\rho}), & \boldsymbol{\rho} \in \Omega_{\mathrm{b}}, \\ \boldsymbol{0}, & \boldsymbol{\rho} \in \Omega_{\mathrm{a}} \setminus \Omega_{\mathrm{b}}, \end{cases} \\
\sum_{vn}(A^{+}_{vn}(z_0) - A^{-}_{vn}(z_0))\boldsymbol{H}^{\mathrm{a}}_{\mathrm{T}vn}(\boldsymbol{\rho}) &= \sum_{vn}(B^{+}_{vn}(z_0) - B^{-}_{vn}(z_0))\boldsymbol{H}^{\mathrm{b}}_{\mathrm{T}vn}(\boldsymbol{\rho}), \quad \boldsymbol{\rho} \in \Omega_{\mathrm{b}}.
\end{aligned} \tag{6.7}$$

To obtain a linear system of equations for the waveguide coefficients, the inner product is taken between Eq. (6.7a) and $\boldsymbol{H}^{\mathrm{a}*}_{\mathrm{T}v'n'}$, and between Eq. (6.7b) and $\boldsymbol{E}^{\mathrm{b}*}_{\mathrm{T}v'n'}$. The following inner product integrals appear

$$\begin{aligned}
\mathbf{Q}^{\mathrm{a}}_{vn,v'n'} &= \int_{\Omega_{\mathrm{a}}} \hat{z} \cdot (\boldsymbol{E}^{\mathrm{a}}_{\mathrm{T}vn} \times \boldsymbol{H}^{\mathrm{a}*}_{\mathrm{T}v'n'})\,\mathrm{dS} = \frac{Y^{\mathrm{a}*}_{vn}}{\eta_0}\delta_{vv'}\delta_{nn'}, \\
\mathbf{Q}^{\mathrm{b}}_{vn,v'n'} &= \int_{\Omega_{\mathrm{b}}} \hat{z} \cdot (\boldsymbol{E}^{\mathrm{b}}_{\mathrm{T}vn} \times \boldsymbol{H}^{\mathrm{b}*}_{\mathrm{T}v'n'})\,\mathrm{dS} = \frac{Y^{\mathrm{b}*}_{vn}}{\eta_0}\delta_{vv'}\delta_{nn'},
\end{aligned} \tag{6.8}$$

and

$$\begin{aligned}
\mathbf{C}_{vn,v'n'} &= \int_{\Omega_{\mathrm{b}}} \hat{z} \cdot (\boldsymbol{E}^{\mathrm{b}}_{\mathrm{T}vn} \times \boldsymbol{H}^{\mathrm{a}*}_{\mathrm{T}v'n'})\,\mathrm{dS} \\
&= \int_{\Omega_{\mathrm{b}}} \boldsymbol{E}^{\mathrm{b}}_{\mathrm{T}vn} \cdot (\boldsymbol{H}^{\mathrm{a}*}_{\mathrm{T}v'n'} \times \hat{z})\,\mathrm{dS} = \frac{Y^{\mathrm{a}*}_{v'n'}}{\eta_0}\int_{\Omega_{\mathrm{b}}} (\boldsymbol{E}^{\mathrm{b}}_{\mathrm{T}vn} \cdot \boldsymbol{E}^{\mathrm{a}*}_{\mathrm{T}v'n'})\,\mathrm{dS}\,.
\end{aligned} \tag{6.9}$$

With these definitions, the linear system for the waveguide coefficients is

$$\begin{cases}
\mathbf{Q}^{\mathrm{a}}(\boldsymbol{A}^{+}(z_0) + \boldsymbol{A}^{-}(z_0)) = \mathbf{C}^{t}(\boldsymbol{B}^{+}(z_0) + \boldsymbol{B}^{-}(z_0)), \\
\mathbf{C}^{*}(\boldsymbol{A}^{+}(z_0) - \boldsymbol{A}^{-}(z_0)) = \mathbf{Q}^{\mathrm{b}*}(\boldsymbol{B}^{+}(z_0) - \boldsymbol{B}^{-}(z_0)).
\end{cases} \tag{6.10}$$

This can be written with a scattering matrix as

$$\begin{pmatrix} \boldsymbol{A}^{-}(z_0) \\ \boldsymbol{B}^{+}(z_0) \end{pmatrix} = \underbrace{\begin{pmatrix} \mathbf{S}^{\mathrm{s}}_{11} & \mathbf{S}^{\mathrm{s}}_{12} \\ \mathbf{S}^{\mathrm{s}}_{21} & \mathbf{S}^{\mathrm{s}}_{22} \end{pmatrix}}_{\mathbf{S}^{\mathrm{s}}} \begin{pmatrix} \boldsymbol{A}^{+}(z_0) \\ \boldsymbol{B}^{-}(z_0) \end{pmatrix}, \tag{6.11}$$

where the elements of the scattering matrix are, see Appendix A.1,

$$\begin{cases}
\mathbf{S}^{\mathrm{s}}_{11} = -(\mathbf{Q}^{\mathrm{a}} + \mathbf{C}^{t}\mathbf{Q}^{\mathrm{b}*-1}\mathbf{C}^{*})^{-1}(\mathbf{Q}^{\mathrm{a}} - \mathbf{C}^{t}\mathbf{Q}^{\mathrm{b}*-1}\mathbf{C}^{*}), \\
\mathbf{S}^{\mathrm{s}}_{12} = 2(\mathbf{Q}^{\mathrm{a}} + \mathbf{C}^{t}\mathbf{Q}^{\mathrm{b}*-1}\mathbf{C}^{*})^{-1}\mathbf{C}^{t}, \\
\mathbf{S}^{\mathrm{s}}_{21} = 2(\mathbf{Q}^{\mathrm{b}*} + \mathbf{C}^{*}\mathbf{Q}^{\mathrm{a}-1}\mathbf{C}^{t})^{-1}\mathbf{C}^{*}, \\
\mathbf{S}^{\mathrm{s}}_{22} = (\mathbf{Q}^{\mathrm{b}*} + \mathbf{C}^{*}\mathbf{Q}^{\mathrm{a}-1}\mathbf{C}^{t})^{-1}(\mathbf{Q}^{\mathrm{b}*} - \mathbf{C}^{*}\mathbf{Q}^{\mathrm{a}-1}\mathbf{C}^{t}).
\end{cases} \tag{6.12}$$

If the smaller waveguide is on the left and the larger waveguide on the right, *cf.* Figure 11(b), the linear system for the waveguide coefficients is

$$\begin{pmatrix} \boldsymbol{A}^{-}(z_0) \\ \boldsymbol{B}^{+}(z_0) \end{pmatrix} = \underbrace{\begin{pmatrix} \mathbf{S}^{\mathrm{g}}_{11} & \mathbf{S}^{\mathrm{g}}_{12} \\ \mathbf{S}^{\mathrm{g}}_{21} & \mathbf{S}^{\mathrm{g}}_{22} \end{pmatrix}}_{\mathbf{S}^{\mathrm{g}}} \begin{pmatrix} \boldsymbol{A}^{+}(z_0) \\ \boldsymbol{B}^{-}(z_0) \end{pmatrix}, \tag{6.13}$$

where the elements of the scattering matrix are, see Appendix A.1,

$$\mathbf{S}^{\mathrm{g}}_{11} = \mathbf{S}^{\mathrm{s}}_{22}, \quad \mathbf{S}^{\mathrm{g}}_{12} = \mathbf{S}^{\mathrm{s}}_{21}, \quad \mathbf{S}^{\mathrm{g}}_{21} = \mathbf{S}^{\mathrm{s}}_{12}, \quad \mathbf{S}^{\mathrm{g}}_{22} = \mathbf{S}^{\mathrm{s}}_{11}. \tag{6.14}$$

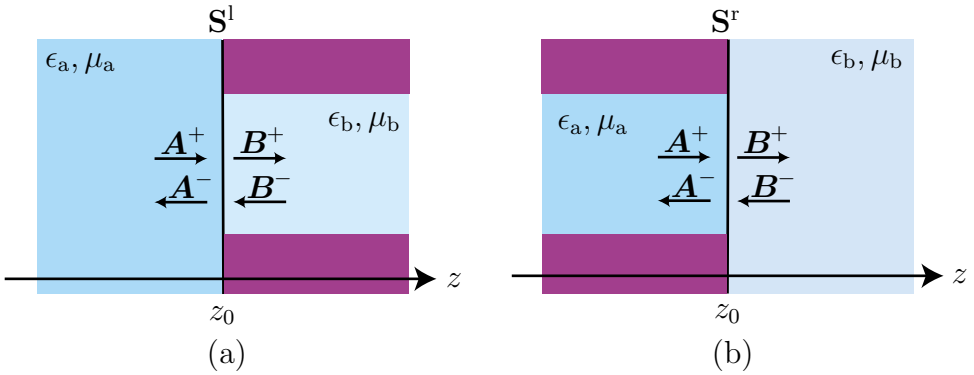

Figure 12: Interface between a dielectric layers and an aperture layers.

6.3 Interface between dielectric and aperture layer

First the case with the dielectric layer to the left and the aperture layer to the right, see Figure 12(a), is studied.

The fields inside the dielectric layer are expanded in Floquet waves as

$$\begin{cases} \boldsymbol{E}^{\mathrm{a}}_{\mathrm{T}}(\boldsymbol{r}) = \sum_{lmn} (a^{+}_{lmn} \mathrm{e}^{\mathrm{i}\gamma^{\mathrm{a}}_{mn} z} + a^{-}_{lmn} \mathrm{e}^{-\mathrm{i}\gamma^{\mathrm{a}}_{mn} z}) \boldsymbol{R}^{\mathrm{a}}_{\mathrm{T}lmn}(\boldsymbol{\rho}), \\ \boldsymbol{H}^{\mathrm{a}}_{\mathrm{T}}(\boldsymbol{r}) = \sum_{lmn} (a^{+}_{lmn} \mathrm{e}^{\mathrm{i}\gamma^{\mathrm{a}}_{mn} z} - a^{-}_{lmn} \mathrm{e}^{-\mathrm{i}\gamma^{\mathrm{a}}_{mn} z}) \boldsymbol{T}^{\mathrm{a}}_{\mathrm{T}lmn}(\boldsymbol{\rho}). \end{cases} \tag{6.15}$$

The fields inside the apertures are expanded in waveguide modes as

$$\begin{cases} \boldsymbol{E}^{\mathrm{b}}_{\mathrm{T}}(\boldsymbol{r}) = \sum_{vn} (b^{+}_{vn} \mathrm{e}^{\mathrm{i}k^{\mathrm{b}}_{zn} z} + b^{-}_{vn} \mathrm{e}^{-\mathrm{i}k^{\mathrm{b}}_{zn} z}) \boldsymbol{E}^{\mathrm{b}}_{\mathrm{T}vn}(\boldsymbol{\rho}), \\ \boldsymbol{H}^{\mathrm{b}}_{\mathrm{T}}(\boldsymbol{r}) = \sum_{vn} (b^{+}_{vn} \mathrm{e}^{\mathrm{i}k^{\mathrm{b}}_{zn} z} - b^{-}_{vn} \mathrm{e}^{-\mathrm{i}k^{\mathrm{b}}_{zn} z}) \boldsymbol{H}^{\mathrm{b}}_{\mathrm{T}vn}(\boldsymbol{\rho}). \end{cases} \tag{6.16}$$

The boundary conditions at the interface $z = z_0$ are enforced. The boundary conditions say that the tangential electric field is continuous over the entire interfaces D, while the magnetic field is continuous over the apertures Ω, *i.e.*,

$$\begin{aligned} \boldsymbol{E}^{\mathrm{a}}_{\mathrm{T}}(\boldsymbol{\rho}, z_0) &= \begin{cases} \boldsymbol{E}^{\mathrm{b}}_{\mathrm{T}}(\boldsymbol{\rho}, z_0), & \boldsymbol{\rho} \in \Omega, \\ \boldsymbol{0}, & \boldsymbol{\rho} \in D \setminus \Omega, \end{cases} \\ \boldsymbol{H}^{\mathrm{a}}_{\mathrm{T}}(\boldsymbol{\rho}, z_0) &= \boldsymbol{H}^{\mathrm{b}}_{\mathrm{T}}(\boldsymbol{\rho}, z_0), \quad \boldsymbol{\rho} \in \Omega. \end{aligned} \tag{6.17}$$

Introducing

$$\begin{aligned} A^{\pm}_{lmn}(z) &= a^{\pm}_{lmn} \mathrm{e}^{\pm \mathrm{i}\gamma^{\mathrm{a}}_{mn} z}, \\ B^{\pm}_{vn}(z) &= b^{\pm}_{vn} \mathrm{e}^{\pm \mathrm{i}k^{\mathrm{b}}_{zn} z}, \end{aligned} \tag{6.18}$$

and enforcing the continuity condition of the field at the interface $z = z_0$ yield

$$\begin{aligned}
&\sum_{lmn}(A^+_{lmn}(z_0) + A^-_{lmn}(z_0))\boldsymbol{R}^{\mathrm{a}}_{\mathrm{T}lmn}(\boldsymbol{\rho}) = \begin{cases} \sum_{vn}(B^+_{vn}(z_0) + B^-_{vn}(z_0))\boldsymbol{E}^{\mathrm{b}}_{\mathrm{T}vn}(\boldsymbol{\rho}), & \boldsymbol{\rho} \in \Omega, \\ \mathbf{0}, & \boldsymbol{\rho} \in D \setminus \Omega, \end{cases} \\
&\sum_{lmn}(A^+_{lmn}(z_0) - A^-_{lmn}(z_0))\boldsymbol{T}^{\mathrm{a}}_{\mathrm{T}lmn}(\boldsymbol{\rho}) = \sum_{vn}(B^+_{vn}(z_0) - B^-_{vn}(z_0))\boldsymbol{H}^{\mathrm{b}}_{\mathrm{T}vn}(\boldsymbol{\rho}), \quad \boldsymbol{\rho} \in \Omega.
\end{aligned} \tag{6.19}$$

To obtain a linear system of equations for the waveguide coefficients, the inner product is taken between Eq. (6.19a) and $\boldsymbol{T}^{\mathrm{a}*}_{\mathrm{T}l'm'n'}$, and between Eq. (6.19b) and $\boldsymbol{E}^{\mathrm{b}*}_{\mathrm{T}v'n'}$. The inner product integrals are

$$\mathbf{R}_{lmn,l'm'n'} = \int_D \hat{z} \cdot (\boldsymbol{R}^{\mathrm{a}}_{\mathrm{T}lmn} \times \boldsymbol{T}^{\mathrm{a}*}_{\mathrm{T}l'm'n'})\,\mathrm{dS} = \frac{Y^{\mathrm{a}*}_{lmn}}{\eta_0}\delta_{ll'}\delta_{mm'}\delta_{nn'}, \tag{6.20}$$

$$\begin{aligned}
\mathbf{Q}_{vn,v'n'} &= \int_\Omega \hat{z} \cdot (\boldsymbol{E}^{\mathrm{b}}_{\mathrm{T}vn} \times \boldsymbol{H}^{\mathrm{b}*}_{\mathrm{T}v'n'})\,\mathrm{dS} \\
&= \int_\Omega \boldsymbol{E}^{\mathrm{b}}_{\mathrm{T}vn} \cdot (\boldsymbol{H}^{\mathrm{b}*}_{\mathrm{T}v'n'} \times \hat{z})\,\mathrm{dS} \\
&= \frac{Y^{\mathrm{b}*}_{v'n'}}{\eta_0}\int_\Omega (\boldsymbol{E}^{\mathrm{b}}_{\mathrm{T}vn} \cdot \boldsymbol{E}^{\mathrm{b}*}_{\mathrm{T}v'n'})\,\mathrm{dS} = \frac{Y^{\mathrm{b}*}_{vn}}{\eta_0}\delta_{vv'}\delta_{nn'},
\end{aligned} \tag{6.21}$$

and

$$\begin{aligned}
\mathbf{C}_{vn,l'm'n'} &= \int_\Omega \hat{z} \cdot (\boldsymbol{E}^{\mathrm{b}}_{\mathrm{T}vn} \times \boldsymbol{T}^{\mathrm{a}*}_{\mathrm{T}l'm'n'})\,\mathrm{dS} \\
&= \int_\Omega \boldsymbol{E}^{\mathrm{b}}_{\mathrm{T}vn} \cdot (\boldsymbol{T}^{\mathrm{a}*}_{\mathrm{T}l'm'n'} \times \hat{z})\,\mathrm{dS} = \frac{Y^{\mathrm{a}*}_{l'm'n'}}{\eta_0}\int_\Omega (\boldsymbol{E}^{\mathrm{b}}_{\mathrm{T}vn} \cdot \boldsymbol{R}^{\mathrm{a}*}_{\mathrm{T}l'm'n'})\,\mathrm{dS}\,.
\end{aligned} \tag{6.22}$$

With these definitions, the linear system for the coefficients is

$$\begin{cases}
\mathbf{R}(\boldsymbol{A}^+(z_0) + \boldsymbol{A}^-(z_0)) = \mathbf{C}^t(\boldsymbol{B}^+(z_0) + \boldsymbol{B}^-(z_0)), \\
\mathbf{C}^*(\boldsymbol{A}^+(z_0) - \boldsymbol{A}^-(z_0)) = \mathbf{Q}^*(\boldsymbol{B}^+(z_0) - \boldsymbol{B}^-(z_0)),
\end{cases} \tag{6.23}$$

which can be written with a scattering matrix as

$$\begin{pmatrix} \boldsymbol{A}^-(z_0) \\ \boldsymbol{B}^+(z_0) \end{pmatrix} = \underbrace{\begin{pmatrix} \mathbf{S}^{\mathrm{l}}_{11} & \mathbf{S}^{\mathrm{l}}_{12} \\ \mathbf{S}^{\mathrm{l}}_{21} & \mathbf{S}^{\mathrm{l}}_{22} \end{pmatrix}}_{\mathbf{S}^{\mathrm{l}}} \begin{pmatrix} \boldsymbol{A}^+(z_0) \\ \boldsymbol{B}^-(z_0) \end{pmatrix}. \tag{6.24}$$

The elements of the scattering matrix are, see Appendix A.1,

$$\begin{cases}
\mathbf{S}^{\mathrm{l}}_{11} = -(\mathbf{R} + \mathbf{C}^t\mathbf{Q}^{*-1}\mathbf{C}^*)^{-1}(\mathbf{R} - \mathbf{C}^t\mathbf{Q}^{*-1}\mathbf{C}^*), \\
\mathbf{S}^{\mathrm{l}}_{12} = 2(\mathbf{R} + \mathbf{C}^t\mathbf{Q}^{*-1}\mathbf{C}^*)^{-1}\mathbf{C}^t, \\
\mathbf{S}^{\mathrm{l}}_{21} = 2(\mathbf{Q}^* + \mathbf{C}^*\mathbf{R}^{-1}\mathbf{C}^t)^{-1}\mathbf{C}^*, \\
\mathbf{S}^{\mathrm{l}}_{22} = (\mathbf{Q}^* + \mathbf{C}^*\mathbf{R}^{-1}\mathbf{C}^t)^{-1}(\mathbf{Q}^* - \mathbf{C}^*\mathbf{R}^{-1}\mathbf{C}^t).
\end{cases} \tag{6.25}$$

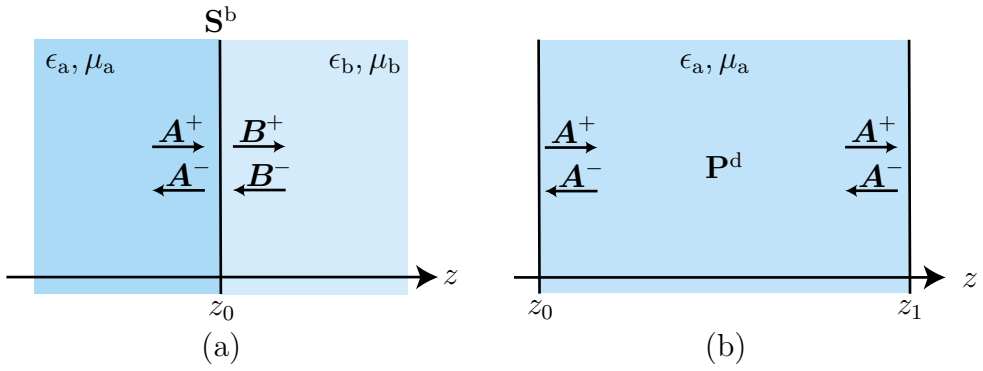

Figure 13: (a) Interfaces between two dielectric layers. (b) Propagation in a dielectric layer.

If the aperture layer is to the left and the dielectric layer to the right, see Figure 12(b), the linear system for the waveguide coefficients are

$$\begin{pmatrix} \boldsymbol{A}^-(z_0) \\ \boldsymbol{B}^+(z_0) \end{pmatrix} = \underbrace{\begin{pmatrix} \mathbf{S}^{\mathrm{r}}_{11} & \mathbf{S}^{\mathrm{r}}_{12} \\ \mathbf{S}^{\mathrm{r}}_{21} & \mathbf{S}^{\mathrm{r}}_{22} \end{pmatrix}}_{\mathbf{S}^{\mathrm{r}}} \begin{pmatrix} \boldsymbol{A}^+(z_0) \\ \boldsymbol{B}^-(z_0) \end{pmatrix}, \tag{6.26}$$

where the elements of the scattering matrix are, see Appendix A.1,

$$\mathbf{S}^{\mathrm{r}}_{11} = \mathbf{S}^{\mathrm{l}}_{22}, \quad \mathbf{S}^{\mathrm{r}}_{12} = \mathbf{S}^{\mathrm{l}}_{21}, \quad \mathbf{S}^{\mathrm{r}}_{21} = \mathbf{S}^{\mathrm{l}}_{12}, \quad \mathbf{S}^{\mathrm{r}}_{22} = \mathbf{S}^{\mathrm{l}}_{11}. \tag{6.27}$$

6.4 Scattering matrix for an interface between two dielectric layers

In the case of an interface between two dielectric layers, see Figure 13(a), the fields inside the dielectric layer are expanded in Floquet waves as

$$\begin{cases} \boldsymbol{E}^{\mathrm{a}}_{\mathrm{T}}(\boldsymbol{r}) = \sum_{lmn} (a^+_{lmn} \mathrm{e}^{\mathrm{i}\gamma^{\mathrm{a}}_{mn} z} + a^-_{lmn} \mathrm{e}^{-\mathrm{i}\gamma^{\mathrm{a}}_{mn} z}) \boldsymbol{R}^{\mathrm{a}}_{\mathrm{T}lmn}(\boldsymbol{\rho}), \\ \boldsymbol{H}^{\mathrm{a}}_{\mathrm{T}}(\boldsymbol{r}) = \sum_{lmn} (a^+_{lmn} \mathrm{e}^{\mathrm{i}\gamma^{\mathrm{a}}_{mn} z} - a^-_{lmn} \mathrm{e}^{-\mathrm{i}\gamma^{\mathrm{a}}_{mn} z}) \boldsymbol{T}^{\mathrm{a}}_{\mathrm{T}lmn}(\boldsymbol{\rho}), \end{cases} \quad z < z_0, \\ \begin{cases} \boldsymbol{E}^{\mathrm{b}}_{\mathrm{T}}(\boldsymbol{r}) = \sum_{lmn} (b^+_{lmn} \mathrm{e}^{\mathrm{i}\gamma^{\mathrm{b}}_{mn} z} + b^-_{lmn} \mathrm{e}^{-\mathrm{i}\gamma^{\mathrm{b}}_{mn} z}) \boldsymbol{R}^{\mathrm{b}}_{\mathrm{T}lmn}(\boldsymbol{\rho}), \\ \boldsymbol{H}^{\mathrm{b}}_{\mathrm{T}}(\boldsymbol{r}) = \sum_{lmn} (b^+_{lmn} \mathrm{e}^{\mathrm{i}\gamma^{\mathrm{b}}_{mn} z} - b^-_{lmn} \mathrm{e}^{-\mathrm{i}\gamma^{\mathrm{b}}_{mn} z}) \boldsymbol{T}^{\mathrm{b}}_{\mathrm{T}lmn}(\boldsymbol{\rho}), \end{cases} \quad z > z_0. \tag{6.28}$$

The boundary conditions at the interface $z = z_0$, that the tangential electric and magnetic fields are continuous over the entire interfaces D, are enforced.

$$\begin{aligned} \boldsymbol{E}^{\mathrm{a}}_{\mathrm{T}}(\boldsymbol{\rho}, z_0) &= \boldsymbol{E}^{\mathrm{b}}_{\mathrm{T}}(\boldsymbol{\rho}, z_0), \quad \boldsymbol{\rho} \in D, \\ \boldsymbol{H}^{\mathrm{a}}_{\mathrm{T}}(\boldsymbol{\rho}, z_0) &= \boldsymbol{H}^{\mathrm{b}}_{\mathrm{T}}(\boldsymbol{\rho}, z_0), \quad \boldsymbol{\rho} \in D. \end{aligned} \tag{6.29}$$

Introducing

$$\begin{aligned} A^{\pm}_{lmn}(z) &= a^{\pm}_{lmn}\mathrm{e}^{\pm \mathrm{i}\gamma^{\mathrm{a}}_{mn}z}, \\ B^{\pm}_{lmn}(z) &= b^{\pm}_{lmn}\mathrm{e}^{\pm \mathrm{i}\gamma^{\mathrm{b}}_{mn}z}, \end{aligned} \tag{6.30}$$

and enforcing the continuity condition of the fields at the interface $z = z_0$ yield

$$\begin{aligned} &\sum_{lmn}(A^{+}_{lmn}(z_0) + A^{-}_{lmn}(z_0))\boldsymbol{R}^{\mathrm{a}}_{\mathrm{T}lmn}(\boldsymbol{\rho}) = \sum_{lmn}(B^{+}_{vn}(z_0) + B^{-}_{lmn}(z_0))\boldsymbol{R}^{\mathrm{b}}_{\mathrm{T}vn}(\boldsymbol{\rho}), \\ &\sum_{lmn}(A^{+}_{lmn}(z_0) - A^{-}_{lmn}(z_0))\boldsymbol{T}^{\mathrm{a}}_{\mathrm{T}lmn}(\boldsymbol{\rho}) = \sum_{lmn}(B^{+}_{vn}(z_0) - B^{-}_{lmn}(z_0))\boldsymbol{T}^{\mathrm{b}}_{\mathrm{T}vn}(\boldsymbol{\rho}). \end{aligned} \tag{6.31}$$

To obtain a linear system of equations for the coefficients, the inner product is taken between Eq. (6.31a) and $\boldsymbol{T}^{\mathrm{a}*}_{\mathrm{T}l'm'n'}$, and between Eq. (6.31b) and $\boldsymbol{R}^{\mathrm{b}*}_{\mathrm{T}l'm'n'}$. The following inner product integrals are defined

$$\begin{aligned} \mathbf{R}^{\mathrm{a}}_{lmn,l'm'n'} &= \int_D \hat{z}\cdot(\boldsymbol{R}^{\mathrm{a}}_{\mathrm{T}lmn}\times\boldsymbol{T}^{\mathrm{a}*}_{\mathrm{T}l'm'n'})\,\mathrm{dS} \\ &= \int_D \boldsymbol{R}^{\mathrm{a}}_{\mathrm{T}lmn}\cdot(\boldsymbol{T}^{\mathrm{a}*}_{\mathrm{T}l'm'n'}\times\hat{z})\,\mathrm{dS} \\ &= \frac{Y^{\mathrm{a}*}_{l'm'n'}}{\eta_0}\int_D(\boldsymbol{R}^{\mathrm{a}}_{\mathrm{T}lmn}\cdot\boldsymbol{R}^{\mathrm{a}*}_{\mathrm{T}l'm'n'})\,\mathrm{dS} = \frac{Y^{\mathrm{a}*}_{lmn}}{\eta_0}\delta_{ll'}\delta_{mm'}\delta_{nn'}, \end{aligned} \tag{6.32}$$

$$\mathbf{R}^{\mathrm{b}}_{lmn,l'm'n'} = \int_D \hat{z}\cdot(\boldsymbol{R}^{\mathrm{b}}_{\mathrm{T}lmn}\times\boldsymbol{T}^{\mathrm{b}*}_{\mathrm{T}l'm'n'})\,\mathrm{dS} = \frac{Y^{\mathrm{b}*}_{lmn}}{\eta_0}\delta_{ll'}\delta_{mm'}\delta_{nn'}, \tag{6.33}$$

and

$$\begin{aligned} \mathbf{C}_{lmn,l'm'n'} &= \int_D \hat{z}\cdot(\boldsymbol{R}^{\mathrm{b}}_{\mathrm{T}lmn}\times\boldsymbol{T}^{\mathrm{a}*}_{\mathrm{T}l'm'n'})\,\mathrm{dS} \\ &= \int_D \boldsymbol{R}^{\mathrm{b}}_{\mathrm{T}lmn}\cdot(\boldsymbol{T}^{\mathrm{a}*}_{\mathrm{T}l'm'n'}\times\hat{z})\,\mathrm{dS} \\ &= \frac{Y^{\mathrm{a}*}_{l'm'n'}}{\eta_0}\int_D(\boldsymbol{R}^{\mathrm{b}}_{\mathrm{T}lmn}\cdot\boldsymbol{R}^{\mathrm{a}*}_{\mathrm{T}l'm'n'})\,\mathrm{dS} = \frac{Y^{\mathrm{a}*}_{lmn}}{\eta_0}\delta_{ll'}\delta_{mm'}\delta_{nn'}. \end{aligned} \tag{6.34}$$

The linear system for the coefficients is

$$\begin{cases} \mathbf{R}^{\mathrm{a}}(\boldsymbol{A}^{+}(z_0) + \boldsymbol{A}^{-}(z_0)) = \mathbf{C}^{t}(\boldsymbol{B}^{+}(z_0) + \boldsymbol{B}^{-}(z_0)), \\ \mathbf{C}^{*}(\boldsymbol{A}^{+}(z_0) - \boldsymbol{A}^{-}(z_0)) = \mathbf{R}^{\mathrm{b}*}(\boldsymbol{B}^{+}(z_0) - \boldsymbol{B}^{-}(z_0)), \end{cases} \tag{6.35}$$

which can be written with a scattering matrix as

$$\begin{pmatrix} \boldsymbol{A}^{-}(z_0) \\ \boldsymbol{B}^{+}(z_0) \end{pmatrix} = \underbrace{\begin{pmatrix} \mathbf{S}^{\mathrm{b}}_{11} & \mathbf{S}^{\mathrm{b}}_{12} \\ \mathbf{S}^{\mathrm{b}}_{21} & \mathbf{S}^{\mathrm{b}}_{22} \end{pmatrix}}_{\mathbf{S}^{\mathrm{b}}} \begin{pmatrix} \boldsymbol{A}^{+}(z_0) \\ \boldsymbol{B}^{-}(z_0) \end{pmatrix}. \tag{6.36}$$

The elements of the scattering matrix are, see Appendix A.1,

$$\begin{cases} \mathbf{S}^{\mathrm{b}}_{11} = -(\mathbf{R}^{\mathrm{a}} + \mathbf{C}^t\mathbf{R}^{\mathrm{b}*-1}\mathbf{C}^*)^{-1}(\mathbf{R}^{\mathrm{a}} - \mathbf{C}^t\mathbf{R}^{\mathrm{b}*-1}\mathbf{C}^*), \\ \mathbf{S}^{\mathrm{b}}_{12} = 2(\mathbf{R}^{\mathrm{a}} + \mathbf{C}^t\mathbf{R}^{\mathrm{b}*-1}\mathbf{C}^*)^{-1}\mathbf{C}^t, \\ \mathbf{S}^{\mathrm{b}}_{21} = 2(\mathbf{R}^{\mathrm{b}*} + \mathbf{C}^*\mathbf{R}^{\mathrm{a}-1}\mathbf{C}^t)^{-1}\mathbf{C}^*, \\ \mathbf{S}^{\mathrm{b}}_{22} = (\mathbf{R}^{\mathrm{b}*} + \mathbf{C}^*\mathbf{R}^{\mathrm{a}-1}\mathbf{C}^t)^{-1}(\mathbf{R}^{\mathrm{b}*} - \mathbf{C}^*\mathbf{R}^{\mathrm{a}-1}\mathbf{C}^t). \end{cases} \tag{6.37}$$

6.5 Propagation matrix for a dielectric layer

Figure 13(b) shows propagation through a dielectric layer. The scattering coefficients on each side of the layer are related to each other as

$$\begin{cases} A^+_{mn}(z_1) = \mathbf{I}\mathrm{e}^{\mathrm{i}\gamma_{mn}(z_1-z_0)}A^+_{mn}(z_0), \\ A^-_{mn}(z_1) = \mathbf{I}\mathrm{e}^{-\mathrm{i}\gamma_{mn}(z_1-z_0)}A^-_{mn}(z_0), \end{cases} \tag{6.38}$$

which can be written in matrix form as

$$\begin{pmatrix} \boldsymbol{A}^-(z_0) \\ \boldsymbol{A}^+(z_1) \end{pmatrix} = \underbrace{\begin{pmatrix} \mathbf{0} & \mathbf{E}^{\mathrm{d}}(z_1 - z_0) \\ \mathbf{E}^{\mathrm{d}}(z_1 - z_0) & \mathbf{0} \end{pmatrix}}_{\mathbf{P}^{\mathrm{d}}} \begin{pmatrix} \boldsymbol{A}^+(z_0) \\ \boldsymbol{A}^-(z_1) \end{pmatrix}, \tag{6.39}$$

where the element of the propagation matrix are

$$\mathbf{E}^{\mathrm{d}}_{mn,m'n'}(z) = \mathrm{e}^{\mathrm{i}\gamma_{mn}z}\delta_{mm'}\delta_{nn'}. \tag{6.40}$$

7 Numerical results

The current method is implemented by a code written in MATLAB. The eigenvalue problem for the waveguide modes was solved by FEMLAB [2]. FEMLAB is a commercial FEM program, which can be integrated in MATLAB as a toolbox.

7.1 Convergence

Since the sets of Floquet modes $\{\boldsymbol{R}_{\mathrm{T}lmn}\}$ and waveguide modes $\{\boldsymbol{E}_{\mathrm{T}vn}\}$ are complete sets and the fields are supposed to be continuous, the expansions of the fields (5.2) and (5.3) are convergent.

A substantial number of evanescent modes must be included in the analysis. This is because the uniform sections will be relatively short in length and thus the amplitude of the decaying modes may still be significant at the next junction.

An important question is: How many Floquet modes and waveguide modes are needed? If the transverse modes are varying equally fast, see Figure 14, we get a good mode matching. The transverse wave number is a good approximation of how fast the transverse modes are varying. The rule is that the maximum of the

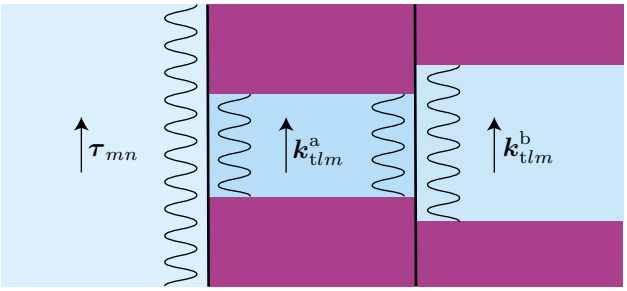

Figure 14: The rule of thumb is that the value of the maximum transverse wave number should be the same in all regions to obtain good mode matching.

transverse wave number in all the layers should be the same. Thus the number of modes in the different layers is determine by, see Figure 14,

$$|\boldsymbol{\tau}_{mn}|_{max} \approx |\boldsymbol{k}^{\mathrm{a}}_{tlm}|_{max} \approx |\boldsymbol{k}^{\mathrm{b}}_{tlm}|_{max}. \tag{7.1}$$

In the numerical examples, the number of the Floquet modes are first fixed and then the number of waveguide modes are determined by Eq. (7.1). The number of Floquet modes are increased until the solution is stable. Floquet mode index up to 8, *i.e.*, $-8 \leq m, n \leq 8$ (see (5.2) and (5.6)), has been used in the numerical examples, this correspond to 578 Floquet modes and approximately 90 waveguide modes.

The numerical waveguide modes are supposed to be reliable, since a thoroughly tested commercial code has been used to calculate the modes. The modes have also been compared to the cases where analytical waveguide modes exist.

7.2 Puck Plate Bandpass Radome

7.2.1 Circular geometry

Figure 15 shows the geometry of a thick-screen Puck Plate (PP) FSS with circular cross-section. The metallic plate is perforated with circular apertures which are partly filled with a dielectric material.

A comparison with predicted results obtained by Wu [12] is depicted in Figure 16. The reflection and transmission are shown at normal incidence ($\theta = 0°$) and at $\theta = 50°$, and the solid lines are calculated by the current method and the dashed lines by Wu. The calculations by the current method agree very well with the results by Wu.

Figure 17 shows the predicted transmission response of this bandpass radome at several incident angles ($\theta = 0°, 30°, 50°, 70°$) for TE- and TM-polarizations. For TE-polarizations, the passband become more narrow and its center frequency decreases when the angle of incidence increases. For TM-polarizations, the passband becomes broader and its center frequency increases when the angle of incidence increases.

The are several features that can be noted; First, the bandwidth of this design is fairly narrow. It can be adjusted by varying the dielectric constant of the load

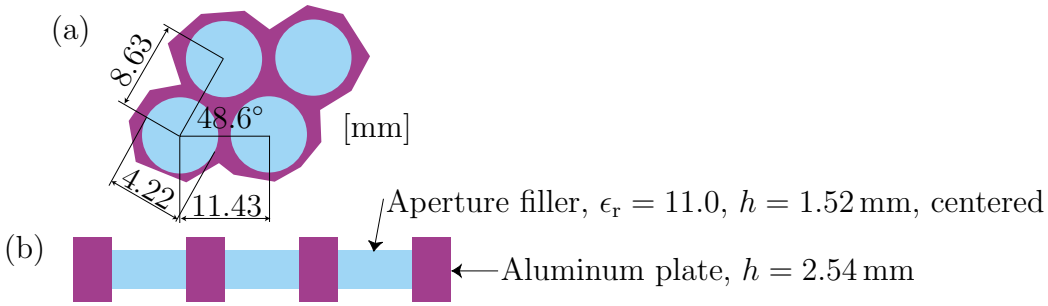

Figure 15: Geometry of the Puck Plate Bandpass FSS.

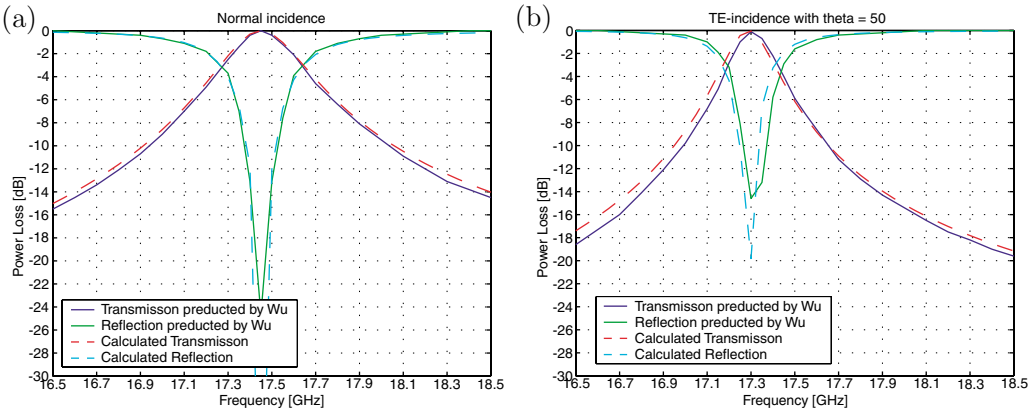

Figure 16: Comparison with predicted results obtained by Wu [12] at normal incidence and at $\theta = 50°$.

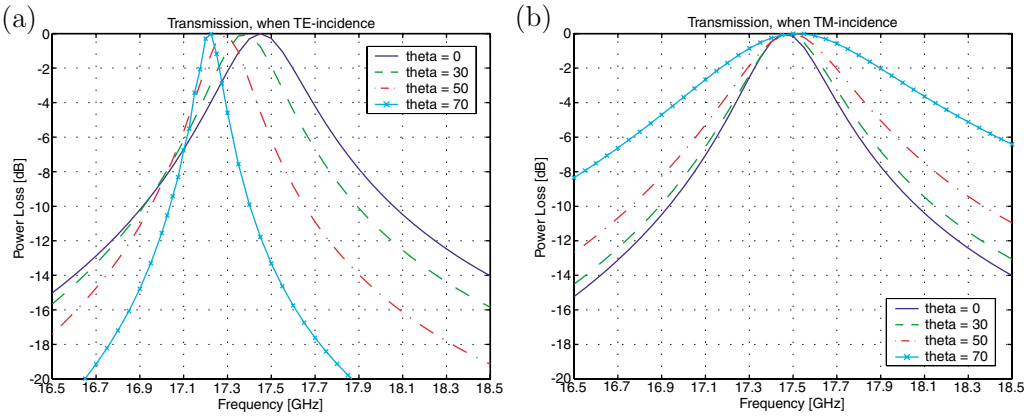

Figure 17: The dependence of the angle of incidence for TE- and TM-incidence for the PP-FSS in Figure 15.

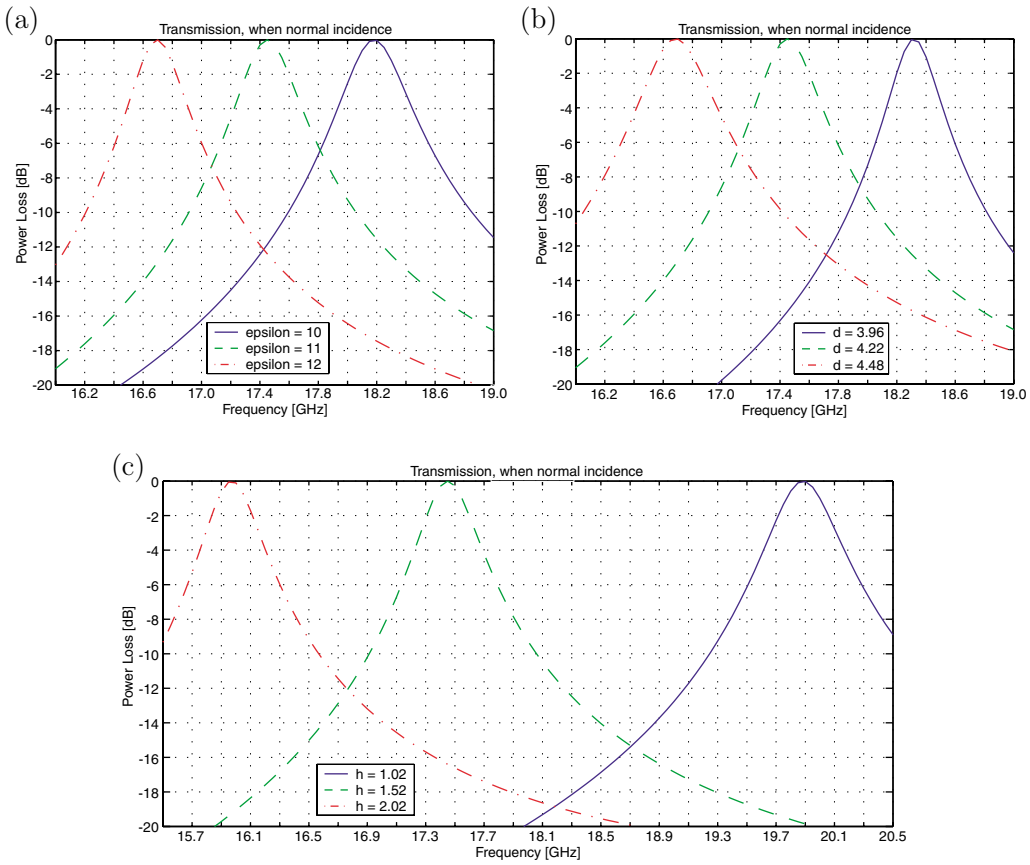

Figure 18: (a) The dependence of the permittivity. (b) The dependence of the diameter of the aperture. (c) The dependence of the thickness of the aperture filler. The geometry of the PP-FSS is in Figure 15.

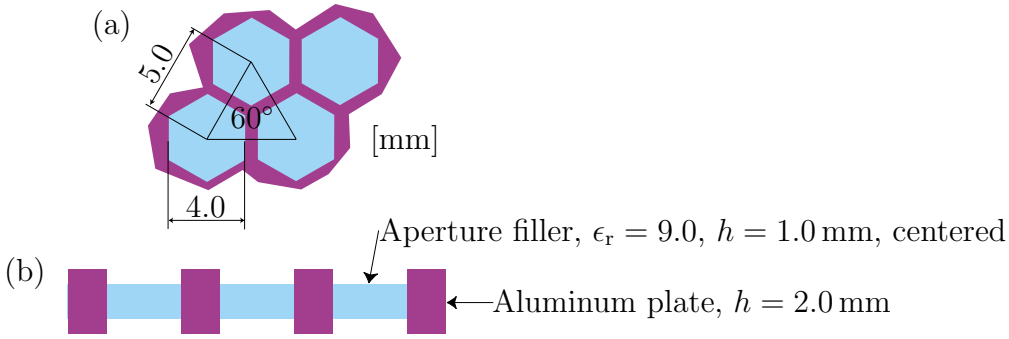

Figure 19: Geometry of the Hexagonal Puck Plate Bandpass FSS.

material, the plate thickness, and the aperture diameter. The resonance of the passband varies with the scan angle and with the polarization of the incident wave. There is no flat passband region because the input impedance of the FSS varies with the angle of incidence and with the polarization. This behavior is typical for this type of thick-screen FSS, when no irises are used in the apertures and no dielectric layers are added to the outside of the conductive thick-screen region to help counteract the effects of the varying input impedance. Because the passband of this thick-screen radome is not stable with the scan angle, it has limited applications where wide scan ability and wide bandwidth are not required.

The dependence of permittivity, diameter and thickness are shown in Figure 18. In (a) it is shown that the passband becomes more narrow and with a center frequency that decreases when the constant of permittivity increases, and in (b) it is shown that the passband becomes broader and with a center frequency that decreases when the diameter of aperture increases. In Figure 18(c) it is shown that the passband becomes more narrow and its center frequency decreases when the thickness of dielectric puck increases.

7.2.2 Hexagonal geometry

In Figure 19 the geometry of a hexagonal Puck Plate Bandpass FSS is depicted. It has almost the same grid and cross-section as in the last example, but now there is a hexagonal cross-section instead of circular. The calculated transmission at different angles of incidence for TE- and TM-polarization are plotted in Figure 20. For TE-polarizations, the passband become more narrow and its center frequency decreases when the angles of incidence increases, and for TM-polarizations, the passband become broader when the angles of incidence increases. The dependence of incident angle for hexagonal apertures is similar to circular apertures, by the dependence are stronger.

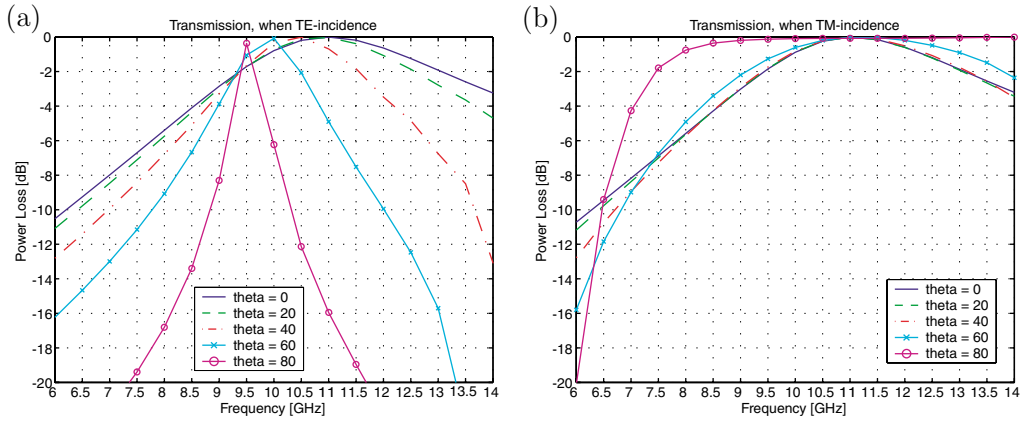

Figure 20: Calculated transmission at different angles of incidence for the PP-FSS in Figure 19.

7.3 The Artificial Puck Plate Radome

7.3.1 Circular geometry

Figure 21 shows the grid and cross-section of an Artificial Puck Plate (APP) FSS with circular cross-section. Irises are included in both apertures and the apertures are filled with dielectric material.

The plots in Figure 22 show calculated transmitted power for four different permittivities of the puck and five different thicknesses of the puck. It is shown, as for PP-FSS, that the passband become more narrow and with a center frequency that decreases when the constant of permittivity increases. The thickness of the puck must be adjusted to fit to the permittivity of the puck. If the thickness is to small, there is a dip between the two resonant frequencies with full transmission, and if the thickness is to large, there is no full transmission at any frequency.

In Figure 23 the calculated reflected and transmitted power for the APP-FSS in Figure 21 are depicted for both TE- and TM-incidence. The reflection and transmission are plotted for a number of different incident angles; $(\theta = 0°, 15°, 30°, 45°, 60°)$. The passband remains stable and is centered around 32.5 GHz. The reflection loss is low for TE-polarization, but for TM-polarization the reflection loss is very large for large angles of incidence. This dependence of incident angle is eliminated by dielectric slabs on either side of the metallic plate.

7.3.2 Wu

Figure 24 shows the geometry of a Ka-band Artificial Puck Plate thick-screen bandpass radome. Irises are included in both apertures and dielectric sheets have been added to the exterior in order to stabilize the scan performance.

Figure 25 shows the measured and calculated, transmission and reflection curves of the Ka-band APP bandpass radome. The plots are done for two different angles of incidence; 15° and 60°. The curves are compared with the results obtained in the

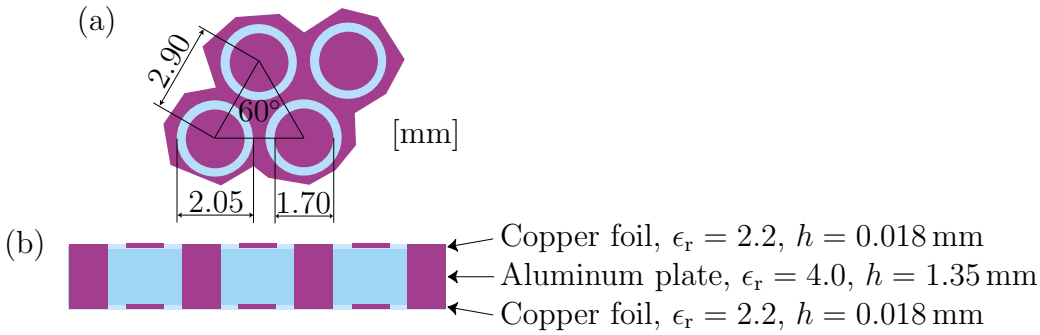

Figure 21: Geometry of the Artificial Puck Plate FSS.

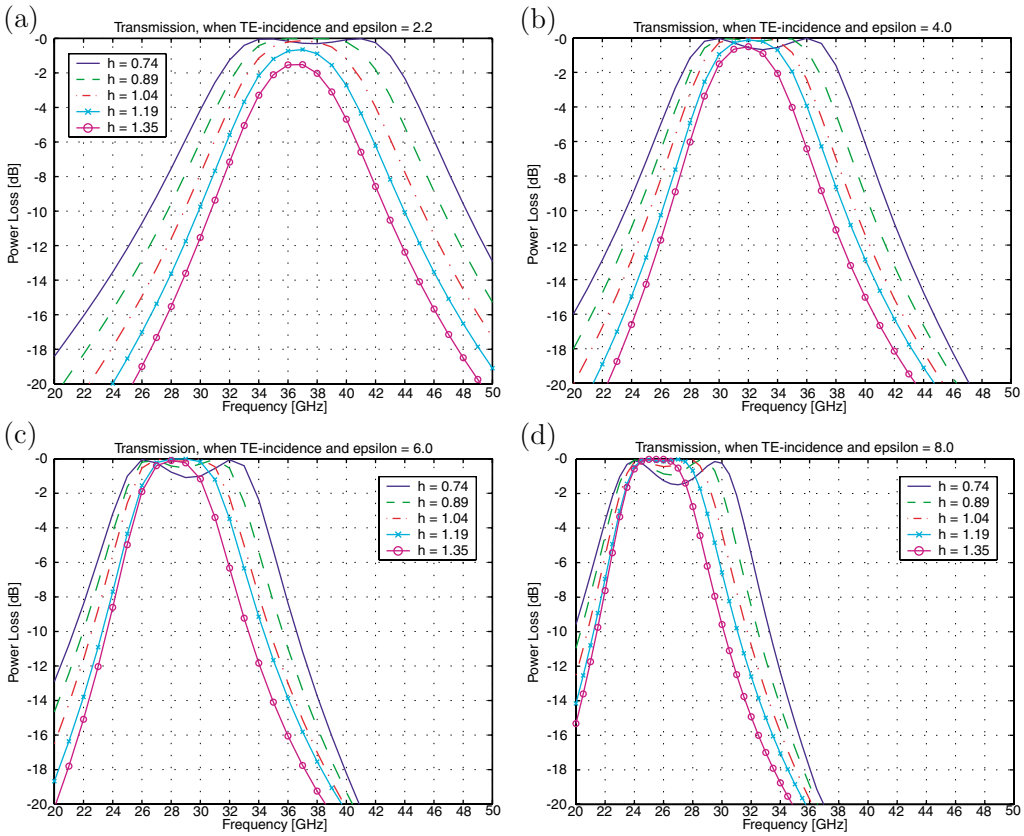

Figure 22: Calculated transmission at different permittivity and thickness for the APP-FSS in Figure 21.

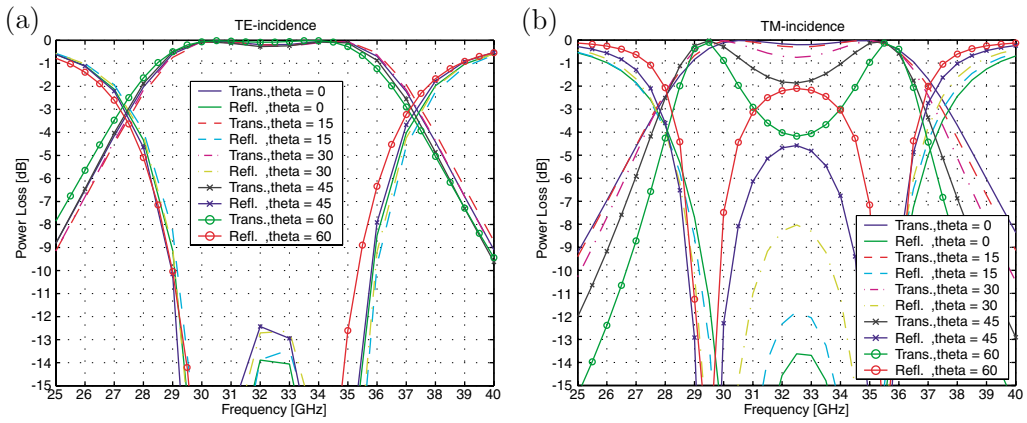

Figure 23: Calculated reflection and transmission of the APP-FSS in Figure 21 at different angles.

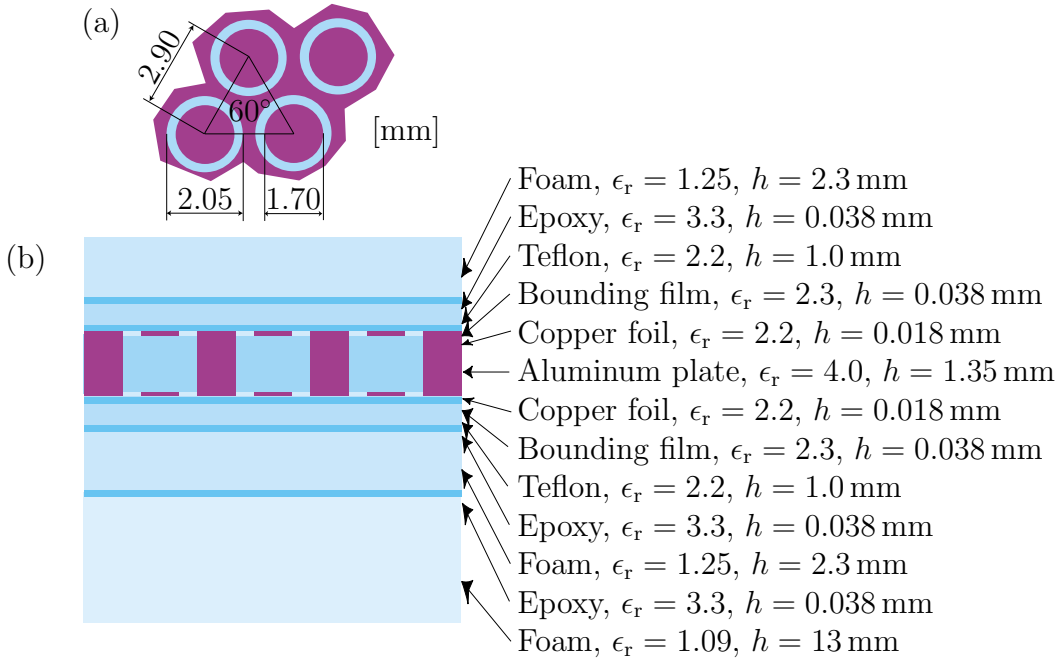

Figure 24: The Grid (a) and Cross-section (b) of the Artificial Puck Plate FSS.

book edited by Wu [12]. The solid lines are calculated by the current method, the dashed and dotted line by Wu and the dots are from measurements. The calculations agree very well with measurements and with the results by Wu.

Figure 26 shows transmission and reflection for incidence between 0° and 60°. The passband remains stable and is centered around 36 GHz. The reflection loss is very low. This performance is ideally suited for applications involving a wide-angle scanning antenna behind a bandpass radome. Note that the bandwidth of this FSS is not extremely high but it meets the requirements for which this radome was designed. The bandwidth can be easily adjusted by changing the dielectric constant of the load material, but more narrow bandwidth yields tighter tolerance and more advanced fabrication techniques.

7.3.3 Hexagonal geometry

In the example in Figure 27 there are almost the same grid and cross-section as in the last example, but now the cross-section is hexagonal. In the last example with the circular cross-section, analytical waveguide modes could have been used, but with the hexagonal cross-section numerical waveguide modes must be use. The waveguide modes are calculated with FEM. The plots in Figure 28 are done for both TE- and TM-incidence, and for five different incident angles; normal incidence, 15°, 30°, 45° and 60°. The curves show that the passband remains stable and the reflection loss is very low.

8 Conclusions

The conclusions from the study is that this method, based on the mode matching technique and the finite element method (FEM), can handle arbitrary frequency selective structures. The result of the method is in accordance with other methods

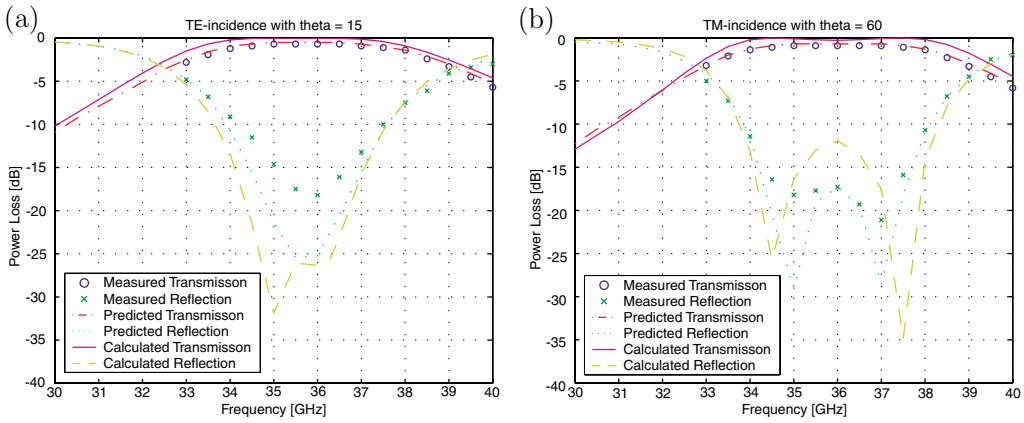

Figure 25: Comparison with measured and predicted, reflection and transmission done by Wu [12] for the FSS in Figure 24.

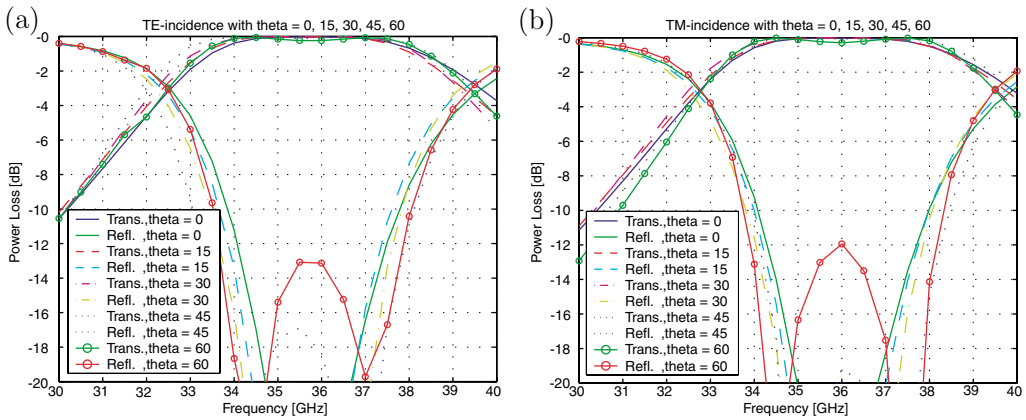

Figure 26: Calculated reflection and transmission at different angles of incidence for the FSS in Figure 24.

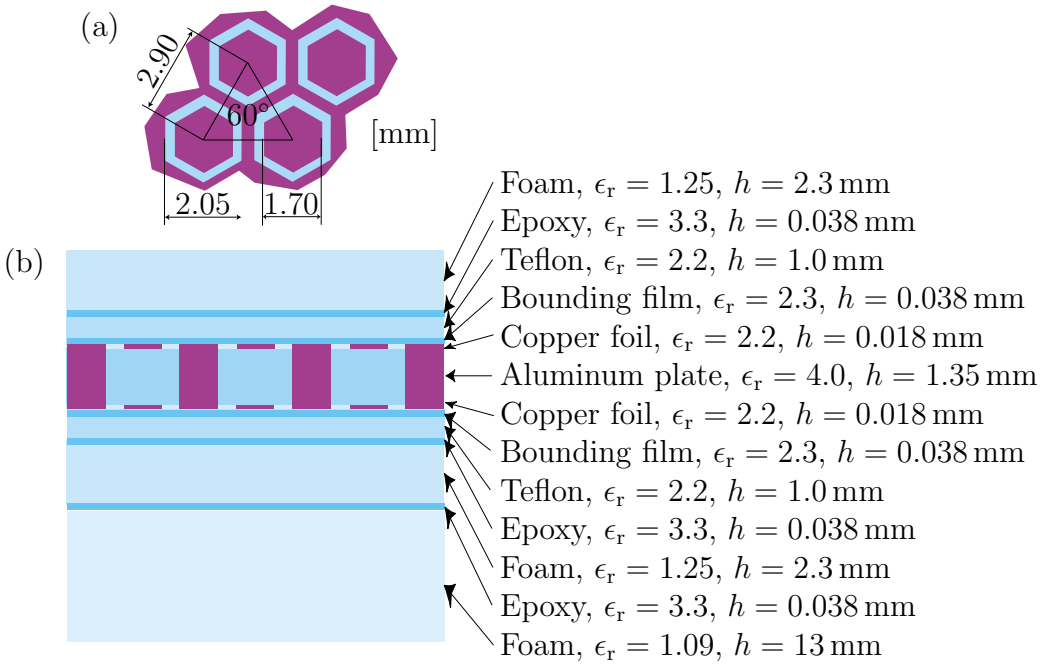

Figure 27: Geometry of the Artificial Puck Plate FSS.

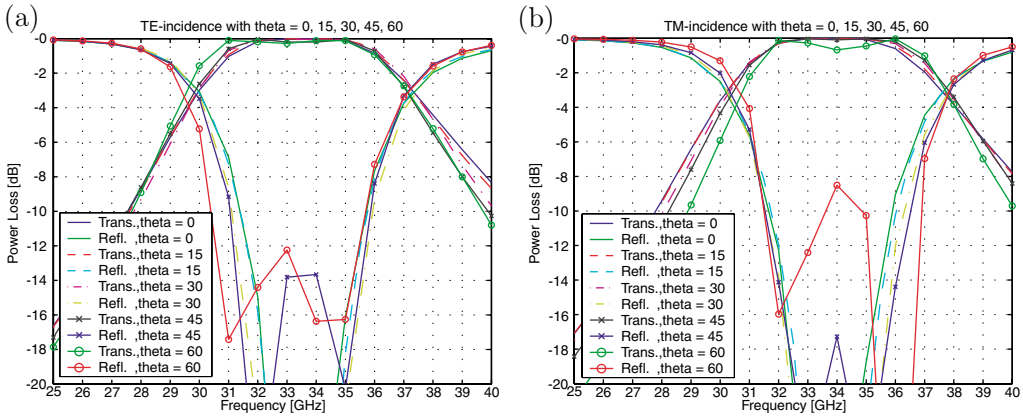

Figure 28: Calculated reflection and transmission at different angles of incidence for the APP-FSS in Figure 27.

and measurements. The result of the present method is also in accordance with the result of an established integral equation method, *i.e.*, the spectral Galerkin method, where the thickness of the screen is assumed to be zero. Hence, the present method can also handle structures with thin-screen FSS.

Irises at the apertures stabilize passband for different incident angles. Dielectric sheets make the FSS independent of the incident angles. The bandwidth decreases when the thickness of the aperture layer is increased and when the permittivity of the aperture layer is increased.

9 Acknowledgments

We would like to thank the Defense Materiel Administration in Sweden for financial support. Furthermore, we would like to thank Sören Poulsen at Celsius Applied Composites AB, ACAB, for reference data to verify our computer code and our results.

Appendix A The linear systems

A.1 The linear system for the waveguide coefficients

The linear system is given by

$$\begin{cases} \mathbf{R}(\boldsymbol{A}^+ + \boldsymbol{A}^-) = \mathbf{C}^t(\boldsymbol{B}^+ + \boldsymbol{B}^-), \\ \mathbf{C}^*(\boldsymbol{A}^+ - \boldsymbol{A}^-) = \mathbf{Q}^*(\boldsymbol{B}^+ - \boldsymbol{B}^-), \end{cases} \tag{A.1}$$

where the sizes of the vectors $\boldsymbol{A}^{\pm}$ and $\boldsymbol{B}^{\pm}$ are n_{a} and n_{b}, respectively. The matrices $\mathbf{R}$ and $\mathbf{Q}$ are quadratic, and the matrix $\mathbf{C}$ is not necessarily quadratic.

The linear system is rewritten as

$$\begin{cases} \boldsymbol{A}^- = \mathbf{R}^{-1}\mathbf{C}^t(\boldsymbol{B}^+ + \boldsymbol{B}^-) - \boldsymbol{A}^+, \\ \boldsymbol{B}^+ = \mathbf{Q}^{*-1}\mathbf{C}^*(\boldsymbol{A}^+ - \boldsymbol{A}^-) + \boldsymbol{B}^-. \end{cases} \tag{A.2}$$

The upper expression is inserted in the lower expression in (A.1), and the lower expression is inserted in the upper expression in (A.1). This gives

$$\begin{aligned} &\begin{cases} \mathbf{R}(\boldsymbol{A}^+ + \boldsymbol{A}^-) = \mathbf{C}^t\mathbf{Q}^{*-1}\mathbf{C}^*(\boldsymbol{A}^+ - \boldsymbol{A}^-) + 2\mathbf{C}^t\boldsymbol{B}^-, \\ 2\mathbf{C}^*\boldsymbol{A}^+ - \mathbf{C}^*\mathbf{R}^{-1}\mathbf{C}^t(\boldsymbol{B}^+ + \boldsymbol{B}^-) = \mathbf{Q}^*(\boldsymbol{B}^+ - \boldsymbol{B}^-), \end{cases} \\ \Leftrightarrow &\begin{cases} (\mathbf{R} + \mathbf{C}^t\mathbf{Q}^{*-1}\mathbf{C}^*)\boldsymbol{A}^- = -(\mathbf{R} - \mathbf{C}^t\mathbf{Q}^{*-1}\mathbf{C}^*)\boldsymbol{A}^+ + 2\mathbf{C}^t\boldsymbol{B}^-, \\ (\mathbf{Q}^* + \mathbf{C}^*\mathbf{R}^{-1}\mathbf{C}^t)\boldsymbol{B}^+ = 2\mathbf{C}^*\boldsymbol{A}^+ + (\mathbf{Q}^* - \mathbf{C}^*\mathbf{R}^{-1}\mathbf{C}^t)\boldsymbol{B}^-, \end{cases} \\ \Leftrightarrow &\begin{cases} \boldsymbol{A}^- = -(\mathbf{R} + \mathbf{C}^t\mathbf{Q}^{*-1}\mathbf{C}^*)^{-1}(\mathbf{R} - \mathbf{C}^t\mathbf{Q}^{*-1}\mathbf{C}^*)\boldsymbol{A}^+ + 2(\mathbf{R} + \mathbf{C}^t\mathbf{Q}^{*-1}\mathbf{C}^*)^{-1}\mathbf{C}^t\boldsymbol{B}^-, \\ \boldsymbol{B}^+ = 2(\mathbf{Q}^* + \mathbf{C}^*\mathbf{R}^{-1}\mathbf{C}^t)^{-1}\mathbf{C}^*\boldsymbol{A}^+ + (\mathbf{Q}^* + \mathbf{C}^*\mathbf{R}^{-1}\mathbf{C}^t)^{-1}(\mathbf{Q}^* - \mathbf{C}^*\mathbf{R}^{-1}\mathbf{C}^t)\boldsymbol{B}^-. \end{cases} \end{aligned} \tag{A.3}$$

The linear system can now be written with a scattering matrix as

$$\begin{pmatrix} \boldsymbol{A}^- \\ \boldsymbol{B}^+ \end{pmatrix} = \begin{pmatrix} \mathbf{S}_{11}^l & \mathbf{S}_{12}^l \\ \mathbf{S}_{21}^l & \mathbf{S}_{22}^l \end{pmatrix} \begin{pmatrix} \boldsymbol{A}^+ \\ \boldsymbol{B}^- \end{pmatrix}, \tag{A.4}$$

where the element of the scattering matrix are

$$\begin{cases} \mathbf{S}_{11}^l = -(\mathbf{R} + \mathbf{C}^t\mathbf{Q}^{*-1}\mathbf{C}^*)^{-1}(\mathbf{R} - \mathbf{C}^t\mathbf{Q}^{*-1}\mathbf{C}^*), \\ \mathbf{S}_{12}^l = 2(\mathbf{R} + \mathbf{C}^t\mathbf{Q}^{*-1}\mathbf{C}^*)^{-1}\mathbf{C}^t, \\ \mathbf{S}_{21}^l = 2(\mathbf{Q}^* + \mathbf{C}^*\mathbf{R}^{-1}\mathbf{C}^t)^{-1}\mathbf{C}^*, \\ \mathbf{S}_{22}^l = (\mathbf{Q}^* + \mathbf{C}^*\mathbf{R}^{-1}\mathbf{C}^t)^{-1}(\mathbf{Q}^* - \mathbf{C}^*\mathbf{R}^{-1}\mathbf{C}^t). \end{cases} \tag{A.5}$$

The sizes of the matrices are

$$\mathbf{S}_{11}^l : n_a \times n_a, \quad \mathbf{S}_{12}^l : n_a \times n_b, \quad \mathbf{S}_{21}^l : n_b \times n_a, \quad \mathbf{S}_{22}^l : n_b \times n_b. \tag{A.6}$$

If the vectors $\boldsymbol{A}$ and $\boldsymbol{B}$ are exchanged in (A.1), the linear system is given by

$$\begin{cases} \mathbf{C}(\boldsymbol{A}^+ + \boldsymbol{A}^-) = \mathbf{R}(\boldsymbol{B}^+ + \boldsymbol{B}^-), \\ \mathbf{Q}^*(\boldsymbol{A}^+ - \boldsymbol{A}^-) = \mathbf{C}^{*t}(\boldsymbol{B}^+ - \boldsymbol{B}^-). \end{cases} \tag{A.7}$$

The matrices $\mathbf{R}$ and $\mathbf{Q}$ are quadratic, but the matrix $\mathbf{C}$ does not have to be quadratic.

The linear system is rewritten as

$$\begin{cases} \boldsymbol{B}^+ = \mathbf{R}^{-1}\mathbf{C}(\boldsymbol{A}^+ + \boldsymbol{A}^-) - \boldsymbol{B}^-, \\ \boldsymbol{A}^- = \boldsymbol{A}^+ - \mathbf{Q}^{*-1}\mathbf{C}^{*t}(\boldsymbol{B}^+ - \boldsymbol{B}^-), \end{cases} \tag{A.8}$$

and the upper expression is inserted in the lower expression in (A.7), and the lower expression is inserted in the upper expression in (A.7). This gives

$$\begin{aligned}
&\begin{cases} 2\mathbf{C}\boldsymbol{A}^+ - \mathbf{C}\mathbf{Q}^{*-1}\mathbf{C}^{*t}(\boldsymbol{B}^+ - \boldsymbol{B}^-) = \mathbf{R}(\boldsymbol{B}^+ + \boldsymbol{B}^-), \\ \mathbf{Q}^*(\boldsymbol{A}^+ - \boldsymbol{A}^-) = -2\mathbf{C}^{*t}\boldsymbol{B}^- + \mathbf{C}^{*t}\mathbf{R}^{-1}\mathbf{C}(\boldsymbol{A}^+ + \boldsymbol{A}^-), \end{cases} \\
\Leftrightarrow &\begin{cases} (\mathbf{R} + \mathbf{C}\mathbf{Q}^{*-1}\mathbf{C}^{*t})\boldsymbol{B}^+ = 2\mathbf{C}\boldsymbol{A}^+ - (\mathbf{R} - \mathbf{C}\mathbf{Q}^{*-1}\mathbf{C}^{*t})\boldsymbol{B}^-, \\ (\mathbf{Q}^* + \mathbf{C}^{*t}\mathbf{R}^{-1}\mathbf{C})\boldsymbol{A}^- = (\mathbf{Q}^* - \mathbf{C}^{*t}\mathbf{R}^{-1}\mathbf{C})\boldsymbol{A}^+ + 2\mathbf{C}^{*t}\boldsymbol{B}^-, \end{cases} \\
\Leftrightarrow &\begin{cases} \boldsymbol{A}^- = (\mathbf{Q}^* + \mathbf{C}^{*t}\mathbf{R}^{-1}\mathbf{C})^{-1}(\mathbf{Q} - \mathbf{C}^{*t}\mathbf{Q}^{-1}\mathbf{C})\boldsymbol{A}^+ + 2(\mathbf{Q}^* + \mathbf{C}^{*t}\mathbf{R}^{-1}\mathbf{C})^{-1}\mathbf{C}^{*t}\boldsymbol{B}^-, \\ \boldsymbol{B}^+ = 2(\mathbf{R} + \mathbf{C}\mathbf{Q}^{*-1}\mathbf{C}^{*t})^{-1}\mathbf{C}\boldsymbol{A}^+ - (\mathbf{R} + \mathbf{C}\mathbf{Q}^{*-1}\mathbf{C}^{*t})^{-1}(\mathbf{R} - \mathbf{C}\mathbf{Q}^{*-1}\mathbf{C}^{*t})\boldsymbol{B}^-. \end{cases}
\end{aligned} \tag{A.9}$$

The linear system can now be written with a scattering matrix as

$$\begin{pmatrix} \boldsymbol{A}^- \\ \boldsymbol{B}^+ \end{pmatrix} = \begin{pmatrix} \mathbf{S}_{11}^l & \mathbf{S}_{12}^l \\ \mathbf{S}_{21}^l & \mathbf{S}_{22}^l \end{pmatrix} \begin{pmatrix} \boldsymbol{A}^+ \\ \boldsymbol{B}^- \end{pmatrix}, \tag{A.10}$$

where the elements of the scattering matrix are

$$\begin{cases} \mathbf{S}_{11}^r = \mathbf{S}_{22}^l = (\mathbf{Q}^* + \mathbf{C}^*\mathbf{R}^{-1}\mathbf{C}^t)^{-1}(\mathbf{Q}^* - \mathbf{C}^*\mathbf{R}^{-1}\mathbf{C}^t), \\ \mathbf{S}_{12}^r = \mathbf{S}_{21}^l = 2(\mathbf{Q}^* + \mathbf{C}^*\mathbf{R}^{-1}\mathbf{C}^t)^{-1}\mathbf{C}^*, \\ \mathbf{S}_{21}^r = \mathbf{S}_{12}^l = 2(\mathbf{R} + \mathbf{C}^t\mathbf{Q}^{*-1}\mathbf{C}^*)^{-1}\mathbf{C}^t, \\ \mathbf{S}_{22}^r = \mathbf{S}_{11}^l = -(\mathbf{R} + \mathbf{C}^t\mathbf{Q}^{*-1}\mathbf{C}^*)^{-1}(\mathbf{R} - \mathbf{C}^t\mathbf{Q}^{*-1}\mathbf{C}^*). \end{cases} \tag{A.11}$$

A.2 The Cascading by Scattering Matrices

The two linear system, which shall be cascaded, are given by

$$\begin{pmatrix} \boldsymbol{A}^- \\ \boldsymbol{B}^+ \end{pmatrix} = \begin{pmatrix} \mathbf{S}_{11}^{\mathrm{a}} & \mathbf{S}_{12}^{\mathrm{a}} \\ \mathbf{S}_{21}^{\mathrm{a}} & \mathbf{S}_{22}^{\mathrm{a}} \end{pmatrix} \begin{pmatrix} \boldsymbol{A}^+ \\ \boldsymbol{B}^- \end{pmatrix} \text{ and } \begin{pmatrix} \boldsymbol{B}^- \\ \boldsymbol{C}^+ \end{pmatrix} = \begin{pmatrix} \mathbf{S}_{11}^{\mathrm{b}} & \mathbf{S}_{12}^{\mathrm{b}} \\ \mathbf{S}_{21}^{\mathrm{b}} & \mathbf{S}_{22}^{\mathrm{b}} \end{pmatrix} \begin{pmatrix} \boldsymbol{B}^+ \\ \boldsymbol{C}^- \end{pmatrix}, \tag{A.12}$$

or equivalently

$$\begin{cases} \boldsymbol{A}^- = \mathbf{S}_{11}^{\mathrm{a}}\boldsymbol{A}^+ + \mathbf{S}_{12}^{\mathrm{a}}\boldsymbol{B}^-, \\ \boldsymbol{B}^+ = \mathbf{S}_{21}^{\mathrm{a}}\boldsymbol{A}^+ + \mathbf{S}_{22}^{\mathrm{a}}\boldsymbol{B}^-. \end{cases} \qquad \begin{cases} \boldsymbol{B}^- = \mathbf{S}_{11}^{\mathrm{b}}\boldsymbol{B}^+ + \mathbf{S}_{12}^{\mathrm{b}}\boldsymbol{C}^-, \\ \boldsymbol{C}^+ = \mathbf{S}_{21}^{\mathrm{b}}\boldsymbol{B}^+ + \mathbf{S}_{22}^{\mathrm{b}}\boldsymbol{C}^-. \end{cases} \tag{A.13}$$

The lower-left expression is inserted in the upper-right expression, and the upper-right expression is inserted in the lower-left. This gives

$$\begin{aligned}
&\begin{cases} \boldsymbol{B}^- = \mathbf{S}_{11}^{\mathrm{b}}\mathbf{S}_{21}^{\mathrm{a}}\boldsymbol{A}^+ + \mathbf{S}_{11}^{\mathrm{b}}\mathbf{S}_{22}^{\mathrm{a}}\boldsymbol{B}^- + \mathbf{S}_{12}^{\mathrm{b}}\boldsymbol{C}^-, \\ \boldsymbol{B}^+ = \mathbf{S}_{21}^{\mathrm{a}}\boldsymbol{A}^+ + \mathbf{S}_{22}^{\mathrm{a}}\mathbf{S}_{11}^{\mathrm{b}}\boldsymbol{B}^+ + \mathbf{S}_{22}^{\mathrm{a}}\mathbf{S}_{12}^{\mathrm{b}}\boldsymbol{C}^-, \end{cases} \\
\Leftrightarrow &\begin{cases} (I - \mathbf{S}_{11}^{\mathrm{b}}\mathbf{S}_{22}^{\mathrm{a}})\boldsymbol{B}^- = \mathbf{S}_{11}^{\mathrm{b}}\mathbf{S}_{21}^{\mathrm{a}}\boldsymbol{A}^+ + \mathbf{S}_{12}^{\mathrm{b}}\boldsymbol{C}^-, \\ (I - \mathbf{S}_{22}^{\mathrm{a}}\mathbf{S}_{11}^{\mathrm{b}})\boldsymbol{B}^+ = \mathbf{S}_{21}^{\mathrm{a}}\boldsymbol{A}^+ + \mathbf{S}_{22}^{\mathrm{a}}\mathbf{S}_{12}^{\mathrm{b}}\boldsymbol{C}^-. \end{cases}
\end{aligned} \tag{A.14}$$

The upper expression is inserted in the upper-left expression in (A.13), and the lower expression is inserted in the lower-right expression in (A.13). This gives

$$\begin{cases} \boldsymbol{A}^- = (\mathbf{S}_{11}^{\mathrm{a}} + \mathbf{S}_{12}^{\mathrm{a}}(I - \mathbf{S}_{11}^{\mathrm{b}}\mathbf{S}_{22}^{\mathrm{a}})^{-1}\mathbf{S}_{11}^{\mathrm{b}}\mathbf{S}_{21}^{\mathrm{a}})\boldsymbol{A}^+ + \mathbf{S}_{12}^{\mathrm{a}}(I - \mathbf{S}_{11}^{\mathrm{b}}\mathbf{S}_{22}^{\mathrm{a}})^{-1}\mathbf{S}_{12}^{\mathrm{b}}\boldsymbol{C}^-, \\ \boldsymbol{C}^+ = \mathbf{S}_{21}^{\mathrm{b}}(I - \mathbf{S}_{22}^{\mathrm{a}}\mathbf{S}_{11}^{\mathrm{b}})^{-1}\mathbf{S}_{21}^{\mathrm{a}}\boldsymbol{A}^+ + (\mathbf{S}_{22}^{\mathrm{b}} + \mathbf{S}_{21}^{\mathrm{b}}(I - \mathbf{S}_{22}^{\mathrm{a}}\mathbf{S}_{11}^{\mathrm{b}})^{-1}\mathbf{S}_{22}^{\mathrm{a}}\mathbf{S}_{12}^{\mathrm{b}})\boldsymbol{C}^-. \end{cases} \tag{A.15}$$

The linear system can now be written with a scattering matrix as

$$\begin{pmatrix} \boldsymbol{A}^- \\ \boldsymbol{C}^+ \end{pmatrix} = \begin{pmatrix} \mathbf{S}^{\mathrm{c}}_{11} & \mathbf{S}^{\mathrm{c}}_{12} \\ \mathbf{S}^{\mathrm{c}}_{21} & \mathbf{S}^{\mathrm{c}}_{22} \end{pmatrix} \begin{pmatrix} \boldsymbol{A}^+ \\ \boldsymbol{C}^- \end{pmatrix}, \tag{A.16}$$

where the elements of the scattering matrix are

$$\begin{cases} \mathbf{S}^{\mathrm{c}}_{11} = \mathbf{S}^{\mathrm{a}}_{11} + \mathbf{S}^{\mathrm{a}}_{12}(I - \mathbf{S}^{\mathrm{b}}_{11}\mathbf{S}^{\mathrm{a}}_{22})^{-1}\mathbf{S}^{\mathrm{b}}_{11}\mathbf{S}^{\mathrm{a}}_{21}, \\ \mathbf{S}^{\mathrm{c}}_{12} = \mathbf{S}^{\mathrm{a}}_{12}(I - \mathbf{S}^{\mathrm{b}}_{11}\mathbf{S}^{\mathrm{a}}_{22})^{-1}\mathbf{S}^{\mathrm{b}}_{12}, \\ \mathbf{S}^{\mathrm{c}}_{21} = \mathbf{S}^{\mathrm{b}}_{21}(I - \mathbf{S}^{\mathrm{a}}_{22}\mathbf{S}^{\mathrm{b}}_{11})^{-1}\mathbf{S}^{\mathrm{a}}_{21}, \\ \mathbf{S}^{\mathrm{c}}_{22} = \mathbf{S}^{\mathrm{b}}_{22} + \mathbf{S}^{\mathrm{b}}_{21}(I - \mathbf{S}^{\mathrm{a}}_{22}\mathbf{S}^{\mathrm{b}}_{11})^{-1}\mathbf{S}^{\mathrm{a}}_{22}\mathbf{S}^{\mathrm{b}}_{12}. \end{cases} \tag{A.17}$$

The sizes of the submatrices are

$$\begin{array}{llll} \mathbf{S}^{\mathrm{a}}_{11} : n_{\mathrm{a}} \times n_{\mathrm{a}}, & \mathbf{S}^{\mathrm{a}}_{12} : n_{\mathrm{a}} \times n_{\mathrm{b}}, & \mathbf{S}^{\mathrm{a}}_{21} : n_{\mathrm{b}} \times n_{\mathrm{a}}, & \mathbf{S}^{\mathrm{a}}_{22} : n_{\mathrm{b}} \times n_{\mathrm{b}}, \\ \mathbf{S}^{\mathrm{b}}_{11} : n_{\mathrm{b}} \times n_{\mathrm{b}}, & \mathbf{S}^{\mathrm{b}}_{12} : n_{\mathrm{b}} \times n_{\mathrm{c}}, & \mathbf{S}^{\mathrm{b}}_{21} : n_{\mathrm{c}} \times n_{\mathrm{b}}, & \mathbf{S}^{\mathrm{b}}_{22} : n_{\mathrm{c}} \times n_{\mathrm{c}}, \\ \mathbf{S}^{\mathrm{c}}_{11} : n_{\mathrm{a}} \times n_{\mathrm{a}}, & \mathbf{S}^{\mathrm{c}}_{12} : n_{\mathrm{a}} \times n_{\mathrm{c}}, & \mathbf{S}^{\mathrm{c}}_{21} : n_{\mathrm{c}} \times n_{\mathrm{a}}, & \mathbf{S}^{\mathrm{c}}_{22} : n_{\mathrm{c}} \times n_{\mathrm{c}}. \end{array} \tag{A.18}$$

References

[1] R. E. Collin. *Field Theory of Guided Waves*. IEEE Press, New York, second edition, 1991.

[2] Computer Solutions Europe AB, Stockholm. *FEMLAB: Reference Manual*, 1998.

[3] J. D. Jackson. *Classical Electrodynamics*. John Wiley & Sons, New York, third edition, 1999.

[4] P. H. Masterman and P. J. B. Clarricoats. Computer field-matching solution of waveguide transverse discontinuities. *Proc. IEE*, **118**, 51–63, 1971.

[5] B. Munk. *Frequency Selective Surfaces: Theory and Design*. John Wiley & Sons, New York, 2000.

[6] A. D. Olver, P. J. B. Clarricoats, A. A. Kishk, and L. Shafai. *Microwave Horns and Feeds*. IEEE Press, New York, 1994.

[7] R. Petit, editor. *Electromagnetic Theory of Gratings*, volume 22 of *Topics in Current Physics*. Springer-Verlag, Heidelberg, 1980.

[8] A. Roberts and R. C. McPhedran. Bandpass grids with annular apertures. *IEEE Trans. Antennas Propagat.*, **36**(5), 607–611, May 1988.

[9] R. G. Schmier, E. W. Lucas, and J. A. Bingham. Frequency selective radome, 1992. Patent number 5,140,338.

[10] A. Wexler. Solution of waveguide discontinuities by modal analysis. *IEEE Trans.*, **15**, 508–517, 1967.

[11] B. Widenberg, S. Poulsen, and A. Karlsson. Scattering from thick frequency selective screens. *J. Electro. Waves Applic.*, **14**, 1303–1328, 2000.

[12] T. K. Wu, editor. *Frequency Selective Surface and Grid Array.* John Wiley & Sons, New York, 1995.